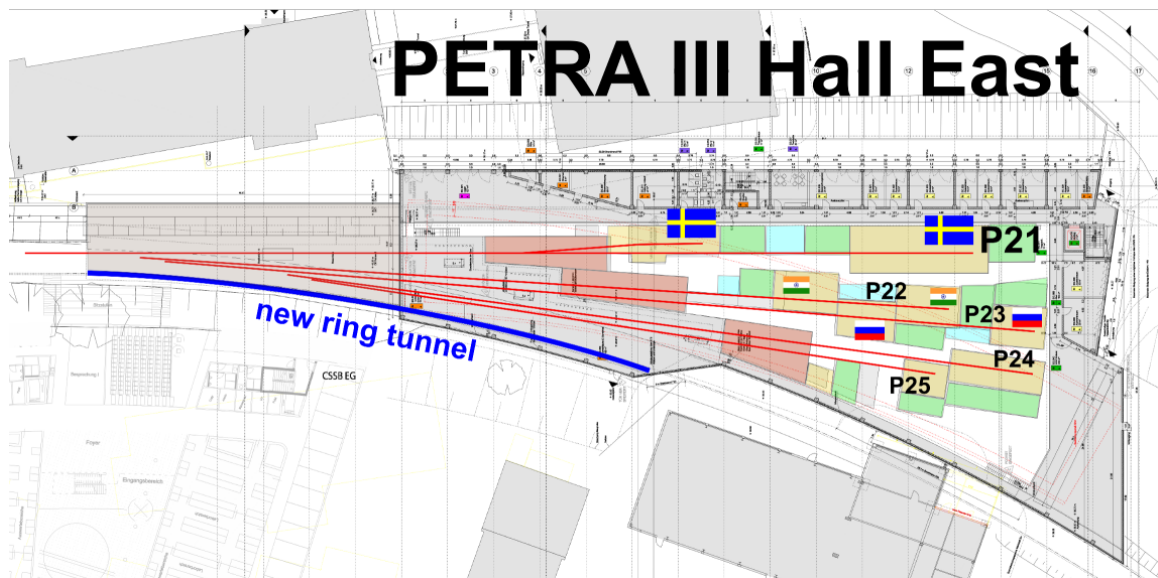# PETRA III Extension Project

Beamline P21:

Swedish High Energy
Materials Science Beamline

Technical Design Report

Final version Aug. 07, 2013

Contributors

DESY Photon Science (FS-PEX)

Ulrich Lienert	Beamline Scientist P21A
Sven Gutschmidt	Beamline Engineer P21A
Martin v. Zimmermann	Beamline Scientist P21B
Rüdiger Nowak	Beamline Engineer P21B
Wolfgang Drube	PETRA III Extension Project Leader

Contents

1   Introduction

1.1   PETRA III Extension Project

DESY is one of the world's leading accelerator centers and a member of the Helmholtz Association, Germany's largest scientific research organization comprising 18 scientific-technical and biological-medical research centers. It develops, builds and operates large particle accelerators used to investigate the structure of matter. Photon science is a major branch of its research activities and DESY has a long standing tradition in the use of synchrotron radiation. For almost 38 years, the 2nd generation facility DORIS served as a very productive high-flux source for synchrotron radiation based research until it was finally shut down in October 2012. Currently, the main photon sources at DESY are the storage ring PETRA III and the Free-Electron-Laser FLASH, offering unique research possibilities for an international scientific community.

PETRA III is a low-emittance (1 nmrad) 6 GeV storage ring evolving from the conversion of the large PETRA accelerator into a 3rd generation light source. Construction started in 2007 and first beamlines became operational in 2009. Today, a total of 14 undulator beamlines are in user operation in the "Max-von-Laue" experimental hall covering 1/8 of the storage ring.

The focus of the facility is on applications making optimum use of the high beam brilliance especially at hard x-ray energies, *i.e.* experiments aiming at nano focusing, ultra-high resolution studies and coherence applications. Because a number of very productive techniques formerly available at DORIS III are not currently implemented at PETRA III and the user demand for access to the new beamlines was anticipated to be very high, it was decided to extend the experimental facilities at the new source and to provide additional beamlines. This PETRA III extension project adds two new experimental halls on either side (North and East) of the current "Max-von-Laue Hall" making use of the long straight sections and part of the adjacent arcs (see Figure 1.1)

Figure 1.1: View of the PETRA III storage ring (red line).
The present experimental hall is shown together with the planned additional experimental halls in the North and East.

The northern straight section already accommodates one of two 40 m long damping wiggler arrays producing an extremely hard and powerful x-ray beam which will also be utilized for materials science experiments. The long straight section in the east is available for additional insertion devices.

In order to accommodate insertion device sources in the arc sections, which currently are filled with long dipole magnets yielding a rather soft X-ray spectrum, the machine lattice will be modified. The new lattice adds double bent achromat (DBA) cells in the arcs, each allowing for a 5 m long straight section. Similar to the present PETRA III beamlines, these straights will serve two beamlines independently by use of canting dipoles resulting in two separate 2 m long straights. Different from the present 5 mrad canting scheme, a canting angle of 20 mrad was chosen at the extension beamlines to provide more spatial flexibility for the experiments further downstream. In total, the new lattice provides eight short straight sections in the two arcs with source properties corresponding to a high-beta section at PETRA III making them very suitable for the use of undulators. Overall, 10 new beamlines will be built.

Five of the new beamlines will be designed as "short undulator" beamlines continuing most of the productive techniques formerly provided at DORIS III bending magnet beamlines. These sources will not only be very well suited for the spectrum of applications to be relocated from DORIS III but also provide a considerably brighter beam. However, some applications specifically took advantage of the comparatively large beam size of a 2nd gen. source. A prominent example is x-ray tomography which was very successfully performed at DORIS wiggler beamlines in an energy range from 7 - 180 keV. Here, the undulator sources at PETRA III are not ideal because of their small beam sizes. One of the new beamlines will make use of the hard X-ray spectrum from the 40 m long damping wiggler array already present in the North, but only a small cross section of this beam can be used because of its extreme power load.

In addition, four high-brilliance undulator beamlines will be built, three in collaboration with international partners, Sweden, India and Russia which will all be located in PETRA III hall East.
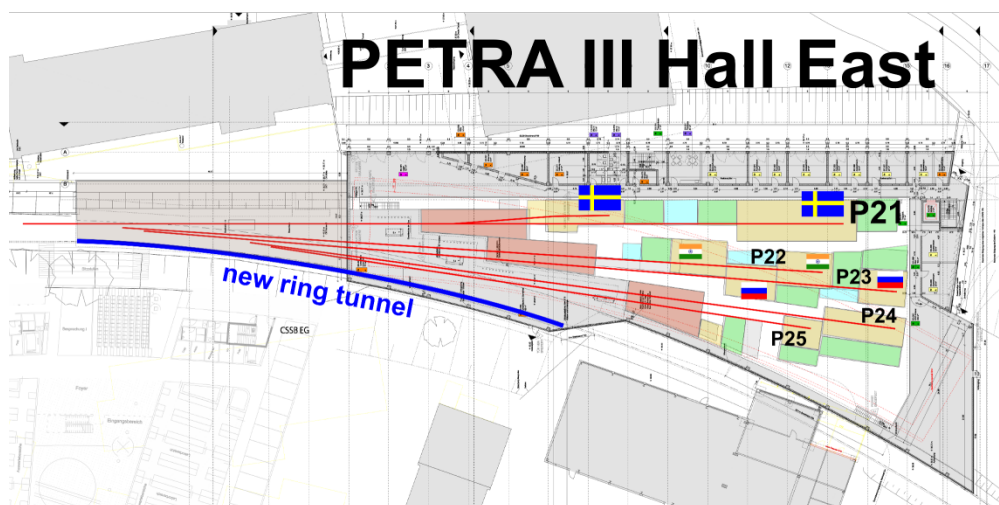

Figure 1.2: Arrangement of the new beamlines in PETRA III hall East.
The section of the storage ring which will be completely rebuilt is indicated.

Since 2009, the science case as well as specifications of the techniques to be implemented are being discussed with the user community, scientific advisory bodies and international partners. A number of specific user workshops have been held. The new beamlines and techniques resulting from this discussion are summarized in Table 1.2 and Table 1.3 below.

A critical issue is the timing of the construction of the extension project because its realization requires a complete shutdown of the current PETRA III user facility for an extended period of time. Also, a prioritization scheme has been defined for a successive implementation of the new beamlines in three phases (see Table 1.1).

Phase 1	Beamlines P64/P65
Phase 2	Beamlines P21-P24
Phase 3	Beamlines P61-P63

Table 1.1: Development phases of the PETRA III extension project.

According to the current schedule, the civil construction of the PETRA III extension will start in January, 2014. During the machine modifications and the initial construction phase of the experimental halls, the storage ring cannot be operated and the user operation at PETRA III will pause. Every effort will be made to minimize this interruption. After the machine restart, the completion of the new facilities PETRA III North and East will continue largely in parallel to the user operation at the present beamlines.

PETRA III East			
beamline	**applications / instruments**	**insertion device**	**range**
P21	high-energy X-ray materials science (Swedish beamline) P21A - high-energy *in-situ* X-ray diffraction and scattering for materials science research - large sample imaging (wiggler) P21B fixed-energy side branch incl. PDF instrument	4 m undulator (in vacuum) 2 m wiggler (in-line) 2 m undulator (canted)	40-150 keV
P22	nano X-ray spectroscopy beamline (India-motivated) - HAXPES relocation from P09 - further X-ray spectroscopy application	2 m undulator	3-50 keV
P23	nano X-ray diffraction (Russian-German collaboration) - structure & processes in low-dimensional and nanoscale systems) - (time-resolved) nano-diffraction in complex and in-situ sample environments - low-T, high-pressure diffraction	2 m undulator	5-50 keV
P24	chemical crystallography - single-crystal diffraction - pump-probe diffraction techniques - diffuse scattering - low temperature & non-ambient sample environments	short undulator	~8-45 keV
P25 (not funded yet)	P25.1 education/training/testing (to be discussed) P25.2 fixed energy side-branch (to be discussed)	short undulator	~4-45 keV

Table 1.2: List of beamlines in the PETRA III extension hall East.

PETRA III North			
beamline	**applications / instruments**	**insertion device**	**range**
P61	P61a high-energy engineering materials science station (Helmholtz-Centre Geesthacht, HZG) P61b extreme conditions (large volume press)	damping wiggler (40 m)	~50-200 keV monochr. & pink beam
P62	small angle X-ray scattering WAXS, SAXS, ASAXS, USAXS in transmission & reflection geometry with moderate beamsize	short undulator	10-35 keV
P63	X-ray micro fluorescence micro-probe applications moderate beam size down to ~5 µm^2	short undulator	4-45 keV
P64	X-ray absorption spectroscopy time-resolved studies & diluted systems QEXAFS (BMBF project, Ronald Frahm, U Wuppertal) bio-XAFS (BMBF project, Gerald Henkel, U Paderborn)	2 m undulator	4-45 keV
P65	X-ray absorption spectroscopy in-situ studies for catalysis & chemistry	short undulator	4-45 keV

Table 1.3: List of beamlines in the PETRA III extension hall North.

1.2   Properties of high energy x-rays

The interaction of high-energy x-rays (typ. 40 – 150 keV) with matter is distinctively different compared to the conventional energy range around 1 Å wavelength. In particular, the attenuation is much reduced and diffraction angles are small (see Figure 1.3). Thus, large momentum transfers can be achieved and large amounts of reciprocal space are compressed into a given solid angle covered by a two-dimensional detector as sketched in Figure 1.4. Also, the diffraction volume can be significantly enlarged enabling the detection of weak and diffuse scattering signals. Over the last decades tremendous progress has been made in the production, focusing, and detection of high-energy synchrotron radiation expanding applications to a wide range of diffraction techniques, including wide angle scattering (WAXS) from micron sized volumes deeply within polycrystalline bulk materials, atomic layers on surfaces and nanometer thin regions of buried interfaces, small angle x-ray scattering, and imaging.

By combination of techniques, length scales from Ångströms to millimeters can be covered with time resolution down to milliseconds and within complex and harsh environments. High-energy synchrotron radiation therefore has become an extremely powerful tool for the *in situ* characterization of materials exposed to external stimuli. The penetration power of neutrons is complemented with high resolution in real and reciprocal space and time.
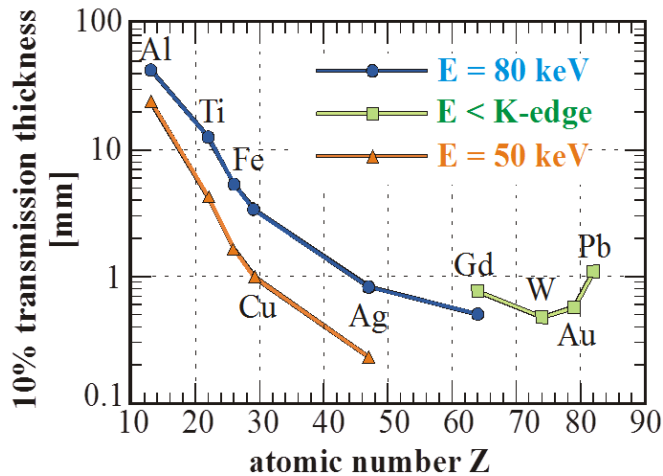
Figure 1.3: Transmission of high-energy x-rays as function of the element Z number.
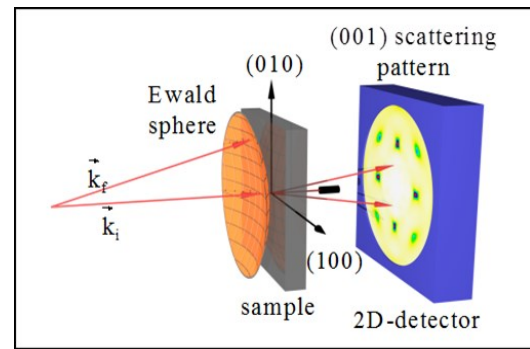

Figure 1.4: Typical high energy diffraction geometry.

1.3 Relevant Workshops

The development of the Swedish High-Energy Materials Science beamline project has been discussed at various workshops involving the German and Swedish partners as well as interested Swedish users (see Table 1.4). An initiating workshop was held in Stockholm in October 2010. The first milestone was the signature of a Memorandum of Understanding between the Swedish Research Council and DESY (Feb. 2011) about the construction of a Swedish Materials Science Beamline within the PETRA III extension project.

The two following scientific workshops (in Stockholm and at DESY) focused on possible fields of applications and suitable instrumentation. In summer 2012, a conceptual design report (CDR) for the beamline was presented by DESY and discussed with the Swedish user community. The initial report also mentioned the possibility of implementing an independent side station using a canted undulator (CU) scheme. The technical feasibility of this concept was shown only recently in fall 2012. In April 2013 a beamline development plan was submitted to the Swedish Research Council.

Workshop and milestone history	
Oct. 25-26, 2010	"Swedish beamline kick-off" workshop, Foresta Hotel, Stockholm
Jun 9-10, 2011	"Brainstorming workshop on ultra-high-energy RIXS", Stockholm
Aug. 29-30, 2011	Workshop on "High energy materials science", DESY, Hamburg
Jun. 25-26, 2012	Scientific workshop, discussion of Conceptual Design Report (CDR), Sigtuna

Table 1.4: Workshop and milestone history.

Scientific scope, experimental techniques and methodologies

Three major scientific interest areas emerged from the workshops: research related to energy materials, structural materials, and atomistic length scale catalysis.

Examples for energy materials include batteries, fuel cells, and hydrogen storage materials. The wider fields of electro-chemistry and chemical crystallography are closely related. The

desired structural descriptors include temporal and spatially resolved identification of crystallographic phases, local order, texture, and lattice strains of statistical averages and individual grains during chemical processes.

Specific examples of structural materials include wear-resistant coatings to improve the efficiency of cutting tools and nano-structured high strength steels. Properties are typically closely related to micro-structural features such as grain size and orientation, grain boundary character, lattice strains and stresses, and cracks and voids. The evolution of these parameters under external stimuli such as thermo-mechanical loading is of crucial importance for the development of predictive models. It is noted that microstructure characterization is also of importance for geological and functional materials.

Studying catalysis on atomistic length scale becomes feasible by achieving sensitivity to mono-atomic layers on single crystal surfaces and by aligning nano-particles on single crystal surfaces. The understanding of fundamental processes will facilitate the development of multifunctional catalytic coatings with enhanced activity. Of key importance is the characterization of catalytic reactions on specific crystallographic surfaces.

In an attempt to matrix the requested capabilities into diffraction instruments and methodologies, a separation into bulk materials, most polycrystalline and some amorphous, and interfaces is most obvious due to the complementary sample positioning requirements. In all cases the importance of *in situ* and *in operando* experiments under external stimuli was emphasized. WAXS covers most of the investigated structural descriptors and is therefore considered as primary technique. However, in many cases combination with small angle x-ray scattering (SAXS) and imaging is desirable to expand length scale coverage.

Methodologies for the characterization of interface diffraction are mainly the reciprocal space mapping of truncation rods and reflectivity measurements. Recently, grazing incidence small angle scattering has been explored. In all cases the experimental control of the small grazing incidence angle is crucial.

Reflecting the variety of micro-structural descriptors, a wide range of methodologies has been developed for the micro-structural characterization of polycrystalline bulk materials. These can be classified into powder diffraction and single grain regimes. Relevant methodologies for the former include the comprehensive characterization of orientation dependencies by pole figure mapping and inversion, and the mapping of 3D spatial heterogeneities by triangulation apertures and tomographic reconstruction of signals obtained from pencil beam diffraction patterns. In the regime of diffraction of individual grains methodologies have been developed to extract grain averaged lattice strains, orientation distributions and therefore five dimensional grain boundary character, and sub-grain formation by high-resolution reciprocal space mapping. Most recently, advanced "dark field microscopy" methodologies are being developed that achieve sub-micron spatial resolution. Local order in nano-crystalline and amorphous materials can be characterized by pair distribution function analysis.

Side-station

Ordering phenomena on short length scales, ranging from a few ten Ångström to a few hundred nanometer have profound influence on materials properties. The determination of

such order is consequently of fundamental importance for understanding these properties and employing them for various functions of these materials. Prominent examples for materials with short range order are glassy systems, nano particle systems, liquids and correlated electron systems with nano scale phase separation.

The methods to study these ordering phenomena are different: For amorphous, nano- and polycrystalline materials pair distribution function (PDF) analysis gives deep insight into the near order structure covering the scattering distribution up to large momentum transfers. The diffuse scattering in correlated electron system related to short range order phenomena can only be studied in single crystals to obtain a high sensitivity.

Both techniques require a heavy load diffractometer in order to carry heavy loads of complex sample environments, which include furnaces, cryomagnets, stress rigs, etc. Probing correlated electron materials the sample is surveyed for small scattering signals due to electronic ordering processes including magnetic scattering. These require sample orientation with three Eulerian angles and a detector device giving a sensitivity of more than eight orders of magnitude, which is achieved by suppression of incoherent background with an analyzer crystal in combination with a point detector. The PDF technique requires a large position sensitive detector to cover high momentum transfers.

Large area tomography

Tomography of centimeter-sized samples using monochromatic synchrotron radiation has become a well-established tool for the non-destructive 3D characterization of materials and artifacts in engineering science, medicine, cultural heritage, zoology and paleontology. At DORIS III wiggler beamlines, rather large samples such as welds, fibre reinforced materials, medical implants with and without the surrounding bone and soft tissue, bone replacement material were routinely investigated using photon energies up to 180 keV. Currently, suitable photon beam sizes are not available at PETRA III undulator beamlines. The possible option to implement an additional wiggler source in the long straight section of PETRA III extension East would allow to complement and extend the capabilities of the present microtomography stations at beamlines P05 and P07, which are well-suited only for small samples. A wiggler source at PETRA III would offer the possibility of both high-spatial and high-density resolution. Furthermore, optimized phase-contrast techniques using partially coherent X-rays could be implemented as well as phase-contrast tomography based on gratings providing new powerful tomographic tools for materials science research.

1.4   Related beamlines at PETRA III

Since the user contract with the Swedish community will provide access to all PETRA III beamlines, a brief overview of relevant existing and planned instruments is given.

Most obvious are synergies with the P07 High-Energy Materials Science beamline. It is planned to install identical in-vacuum undulators at P21 and P07 such that the source parameters will be identical except for slightly different beta-functions and the availability of a low beta-mode at P07. The first experimental station of P07 is operated by DESY and is dedicated to high-energy physics experiments. Most notably, it is equipped with an interface

diffractometer which enables nano-radian control of the grazing incidence angle (cf. section 5.4.2).

The instrument is being operated very successfully but clearly cannot meet the additional demands of the Swedish user community in terms of beamtime. It is therefore proposed to implement a copy of the instrument at the Swedish beamline. Significant synergies can be attained by specializing optics, sample environments, detectors, and secondary techniques. A detailed plan is under discussion, potential complementarities and specialization include: the P07 instrument is less than half the distance from the source compared to a P21 instrument, indicating that the former should provide more flux and the latter smaller focus size and lower divergence. No plans exist to duplicate the monochromator for liquid interfaces at P07. A dedicated SAXS camera is planned for P21 and a large area detector with an opening for the direct beam. Furthermore, a detector with high dynamic range is considered for P21.

The other experimental stations at P07 are operated by the Helmholtz-Zentrum Geesthacht (HZG). The next experimental hutch (EH), EH3, is equipped with a hexapod and moveable detector portal. The hexapod provides the ability to position loads up to 1 t to micrometer precision and a low precision vertical rotation axis and limited tilts. Furthermore, free floor space is reserved to accommodate very heavy and bulky instrumentation. The detector portal provides maximum flexibility but limited translation range and requires manual pre-positioning. Accordingly, the station is very suitable to operate bulky sample environments but setups require manual pre-alignment.

The last experimental station, EH4, is equipped with two instruments, upstream a "grain mapper" and an imaging instrument downstream. The grain mapper is optimized to minimize positional drifts between focusing elements, sample positioning, and near- and far-field detectors while the load capacity of the air-bearing stage is limited to 20 kg. A near-field "compound-detector" is available that provides simultaneous detection at two near-field distances but severely constrains the dimensions of sample environment. Combination with high resolution reciprocal space mapping and SAXS are not foreseen. Like the grain-mapper, the imaging setup is a self-contained instrument, featuring in particular a versatile and carefully designed detector. However, combination with far-field WAXS is presently not possible.

The P02 beamline has a side branch dedicated to high-resolution powder diffraction using a multi-crystal analyzer, and faster but lower resolution powder diffraction and PDF measurements using a large area detector. The optics consists of two flat Laue crystals delivering a bandwidth of 2×10^{-4} at a fixed energy of 60 keV. The optics and instrumentation are complementary to the proposed plans for P21.

Beamline P61 (PETRA III extension North) should be served by a 40 m long damping wiggler with a critical energy of 35.8 keV. Due to the excessive heat load only 3×2 mm^2 (h $\times$ v) beam can be accepted. While detailed plans have not yet been worked out, it is planned that HZG will operate a monochromatic and white beam compatible end station for engineering applications. The nature of the damping wiggler source strongly suggests flux optimizing optics and white beam techniques, whereas focusing is a central theme at P21. It is also noted that no technically feasible solution was found to efficiently operate a side station from the damping wiggler source.

1.5   Beamline design guidelines

First priority is the accommodation of the experimental techniques requested by the Swedish user community as summarized in section 1.3. Next, the particular setting of P21 (long straight section and large total length of the beamline) and the capabilities and capacities of relevant existing and planned PETRA III beamlines are considered, including opportunities to accommodate the related broad band single crystal diffraction and wide beam tomography techniques. Unique opportunities arise from the availability of two 5 m sections for insertion devices of which one can be split to accommodate a canted and an in-line 2 m long insertion device. It is proposed to install a 4 m long in-vacuum undulator in the other section that will provide exceptional brilliance at high energies and manageable heat load.

An energy range of 40-150 keV is proposed since it should cover the experimental requests and would extend the energy range that can be effectively covered at MAX IV. Next, technically incompatible requirements must be separated. This leads to a partition into heavy load sample environments (beyond about 100 kg) and (sub-) micrometer positioning, in particular when a precision rotation axis is included. It is proposed that a heavy load diffractometer is located in a side station as described below.

Bulk and interface diffraction

While the diffraction from bulk materials and interfaces require complementary sample positioning, they share the need of micro-focusing, combination of wide and small angle scattering, and high performance far-field detectors. Instead of an organization into dedicated instruments consisting of (focusing) optics, sample positioning (and environments), and detectors, a modular setup is proposed where all optical elements, sample positioning units, and detectors can be combined. However, it is crucial that the components are "pre-aligned" to minimize the setup effort and optimize data quality. Well defined components are also a prerequisite to advance the automation of alignment procedures which is considered key to an efficient beamline operation. A modular structured diffraction station would also enable "zoom-in" data acquisition by combining diffraction and imaging capabilities. The proposed instrumentation of the diffraction station should enable a wide range of the methodologies described in section 1.3. The priorities of the actual implementation and development of methodologies will be driven by user demand and contributions.

In conclusion, a modular structured diffraction station is proposed for bulk and interface diffraction. Particular capabilities will be the combination of wide angle scattering with small angle scattering and imaging. This also will maximize synergies with the P07 beamline which is mostly structured into instruments.

The diffraction station should be located on the in-line branch for best possible focusing. Due to the complex instrumentation it should be at the downstream end to enable access for setup, development, and maintenance while experiments are performed in an upstream station. A large source distance also maximizes the ratio of the largest to smallest beam size and is therefore beneficial for "zoom-in" data acquisition. The only drawback is a relative short distance from the sample to the SAXS detector of about 6 m. Options considered to increase the distance to the SAXS detector are to extend the EH3 on cost of the EH2, and to extend EH3 downstream and move the CH3 on top of the EH3 extension.

Wide-beam tomography

A wiggler is proposed as one of the two insertion devices for the split 5 m section. Due to the wide beam fan the wiggler monochromator must diffract in the vertical scattering plane and therefore serve another in-line station. This station will be just upstream of the diffraction station. Since tomography instruments are exceptionally self-contained it is reasonable to foresee that a tomography instrument could be removed from the hutch to provide space for bulky sample environments such as sample synthesis chambers. This functionality is referred to as "roll-in" station. It is noted that the "roll-in" station can be served both from the wiggler and undulator.

Broad band diffraction

Finally, it is proposed that an independent side-station that will be served by the canted 2 m undulator will accommodate the broad band single crystal diffraction and PDF programs. It will be equipped with a heavy load sample stage such that high field magnets could be mounted. An optical solution to prevent excessive beam broadening due to the large bandwidth is proposed.

1.6   Beamline overview

For the convenience of the reader, figures providing a beamline overview are compiled while technical details are given in subsequent sections.
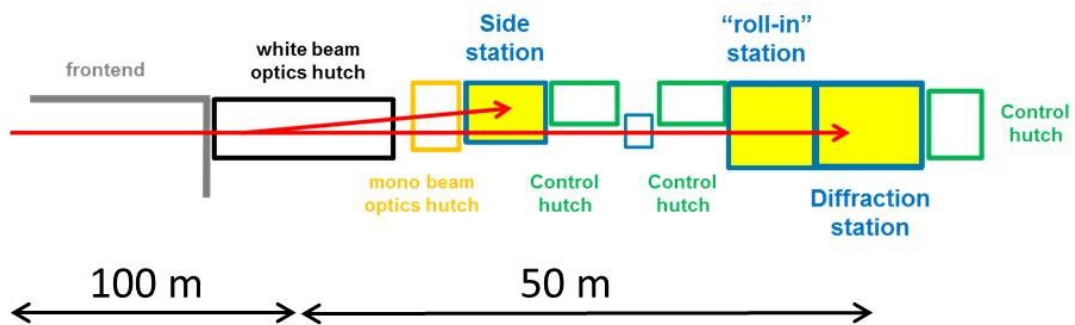

Figure 1.5: Sketch of the principle beamline layout.
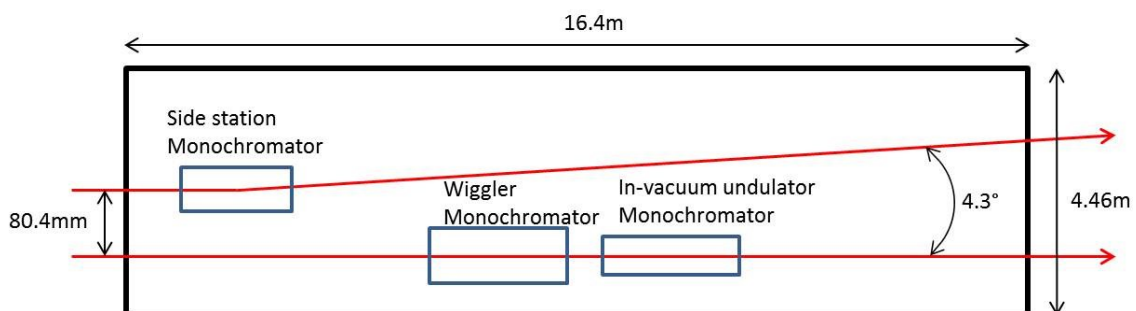**The arrangement of the insertion devices is sketched Figure 2.1.**

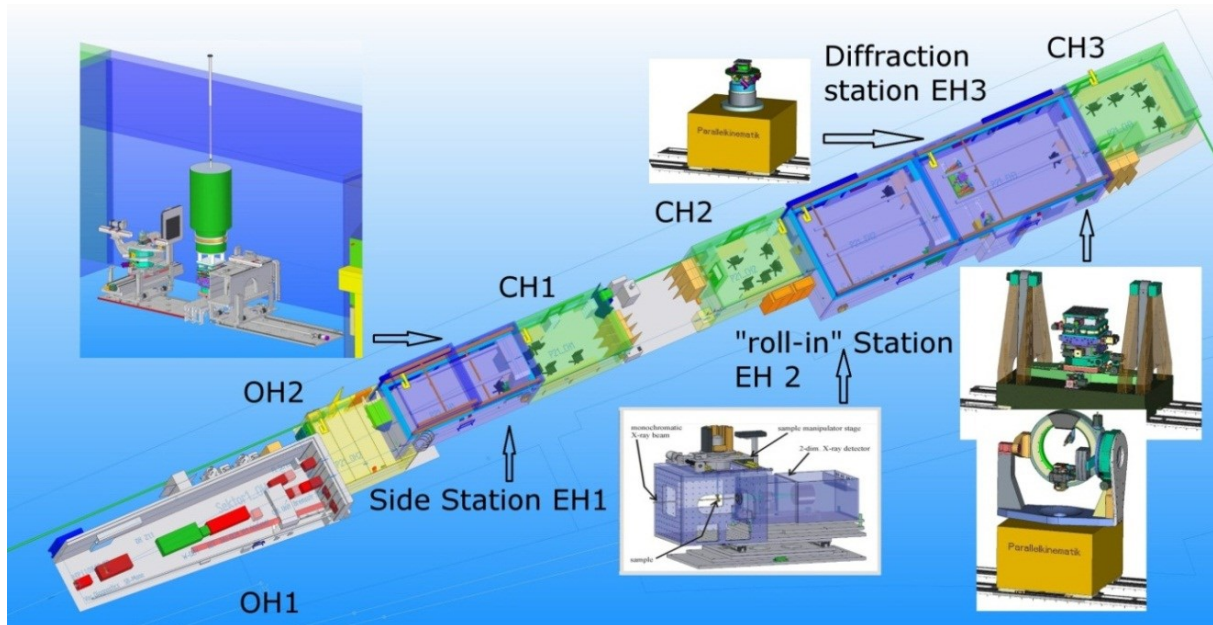**Figure 1.6: Arrangement of monochromators in the white beam optics hutch (OH1).**

Figure 1.7: 3D model of the present beamline design status.

IDs			EH1 (side station)	Length = 8.6 m	
Canted Undulator	12 m	IVU	Entrance	99.9 m	CU
Wiggler	16 m	IVU	Sample position	102.8 m	CU
OH1	Length = 16.4 m		**CRL enclosure**	Length = 1.5 m	
Entrance	90.9 m	IVU	Entrance	131.9 m	IVU
Side branch mono	80.9 m	CU			
Wiggler mono	81.7 m	W	**EH2**	Length = 8.2 m	
IVU mono	100.3 m	IVU	Entrance	122.4 m	W
In-line CRLs	103.9 m	IVU			
Side-branch CRLs	91.9 m	CU	**EH3**	Length = 9.8 m	
			Entrance	146.6 m	IVU
OH2	Length = 4.76 m		Sample position	149.9 m	IVU
Entrance	107.3 m	IVU	SAXS detector	155.9 m	IVU
2nd crystal	99.1 m	CU			
High resolution mono	109.7 m	IVU			

Table 1.5: Distances of selected beamline components from their respective source point: IVU (red), CU (blue) and wiggler (green).

1.7   Beamline development phases

The development of the beamline instrumentation is structured into three phases reflecting the priorities of the relevant programs and technical constraints. A strictly progressive structuring would conflict with efficient implementation, for instance the machine vacuum system will only be modified once and must be designed to be compatible with all insertion devices, likewise all experimental hutches will be constructed simultaneously.

Phase I

A central objective of phase I is an early availability of a brilliant high-energy x-ray beam for user experiments in the diffraction station. The storage ring components will be configured to be compatible with the operation of all three insertion devices but only the in-vacuum undulator will be installed initially, constrained by the limitations of available frontend components. All optics-, experimental-, and control-hutches and supply infrastructure will be completed since progressive construction is not practical. The in-vacuum undulator beam will serve the diffraction station (EH3) equipped with initial instrumentation suitable to perform basic diffraction experiments. Full functionality of the instrumentation will be implemented during phase II.

Phase	Instrumentation	Functionality	First availability
I	• In-vacuum undulator • In-line undulator frontend and monochromator • (Prelim.) side station monochromator • All hutches & infrastructure • Essential instrumentation in the diffraction & side stations	• High-Energy materials diffraction (basic) • "parasitic" operation of heavy load diffractometer and PDF instrument	early 2016
II	• Canted undulator • Canted undulator frontend • Side station monochromator • Fully developed instrumentation in the diffraction & side stations	• Independent operation of heavy load diffractometer and PDF instrument • "roll-in" instruments with undulator • High-Energy materials diffraction (advanced)	Summer 2017
III	• In-line wiggler • wiggler frontend • wiggler monochromator	• Wide beam tomography	>2017

Table 1.6: Synopsis of instrumentation and functionality of the beamline development phases.

Simultaneously, the side station can be served in a "parasitic" mode from the in-line undulator beam. This would enable commissioning of the side station instrumentation and also first scientific experiments, overall providing significantly more user beamtime at the Swedish beamline.

Phase II

In phase II, the canted undulator will be installed and the frontend components be modified such that both undulator beams can be independently delivered into the optics hutch. The final side branch monochromator will be installed such that the side- and in-line stations can be operated simultaneously and independently.

Furthermore, the "roll-in" station (EH2) will be instrumented and the instrumentation development of the diffraction station will continue, with increasing focus on sample environment. The equipment must be compatible with high-energy diffraction geometries

such that custom designs will be required in most cases. Staging the development will allow to take into consideration opportunities and constraints by the phase I instrumentation and smooth out engineering demand.

Phase III

Finally, the wiggler will be installed and – if necessary in the final design – further frontend components may have to be modified. The wiggler monochromator will be installed in the optics hutch and "wide-beam techniques" such as tomography can be performed in the "roll-in" station.

2   Insertion devices

The beamline will be served from a 108 m long straight section providing the unique opportunity to install three insertion devices. A 4 m long short period in-vacuum undulator and a 2 m long wiggler are proposed to serve the in-line diffraction and "roll-in" stations, respectively. Furthermore, a canted 2 m undulator is proposed to serve the side station. All simulations presented in this chapter were calculated with the program SPECTRA (Tanaka & Kitamura, 2001). An energy spread of 0.0011 was included but no magnetic field errors.

2.1   Electron beam parameters & canting scheme

The long straight section has two about 5 m long sub-sections with low dispersion which are suitable for the installation of insertion devices. Only high-beta mode is provided and the electron beam parameters are summarized in Table 2.1.

	x_{rms}	x_{fwhm}	y_{rms}	y_{fwhm}
emittance, ε	1 nm rad		0.01 nm rad	
β function	20 m		3.5 m	
beam size, σ	141 μm	333 μm	5.92 μm	13.9 μm
beam divergence, σ'	7.07 μrad	16.7 μrad	1.69 μrad	3.98 μrad

Table 2.1: Electron beam parameters at the P21 ID sections.

The arrangement of the proposed insertion devices is shown in Figure 2.1. The in-vacuum undulator is planned for phase I, the canted undulator for phase II, and the wiggler for phase III.
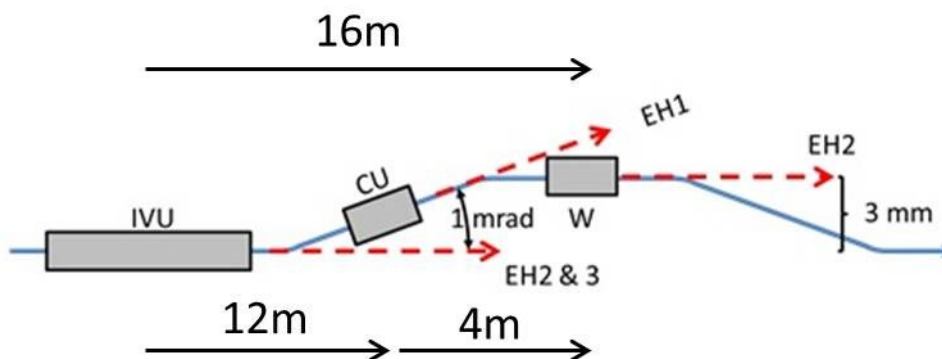

Figure 2.1: Principal sketch of the proposed arrangement of the insertion devices
(IVU: in-vacuum undulator, CU: canted undulator, W: wiggler), blue: electron beam, red: x-ray beams.

2.2   In-vacuum undulator

The key performance parameters that need to be considered for the optimization of a high-energy undulator are the brilliance, tunability, and total power. Shorter periods boost the brilliance of low order harmonics, minimize the total power, but also limit tunability, while large magnetic fields promote the opposite trends. The in-vacuum operation of an undulator is particularly beneficial in the high-energy regime since short magnetic periods can produce significant magnetic fields. The field of relevant hybrid magnets can be approximated by (Balewski *et al.*, 2004)

$$B_0 = a \cdot exp\left(b\,\frac{g}{\lambda_U} + c\left(\frac{g}{\lambda_U}\right)^2\right) \tag{2.1}$$

where g and λ_U are the gap and period of the undulator, and the factors a, b, c are taken as 3.694, -5.068, 1.52, respectively. Figure 2.2 shows a comparison of on-axis brilliance for different periods and a minimum gap of 7 mm.
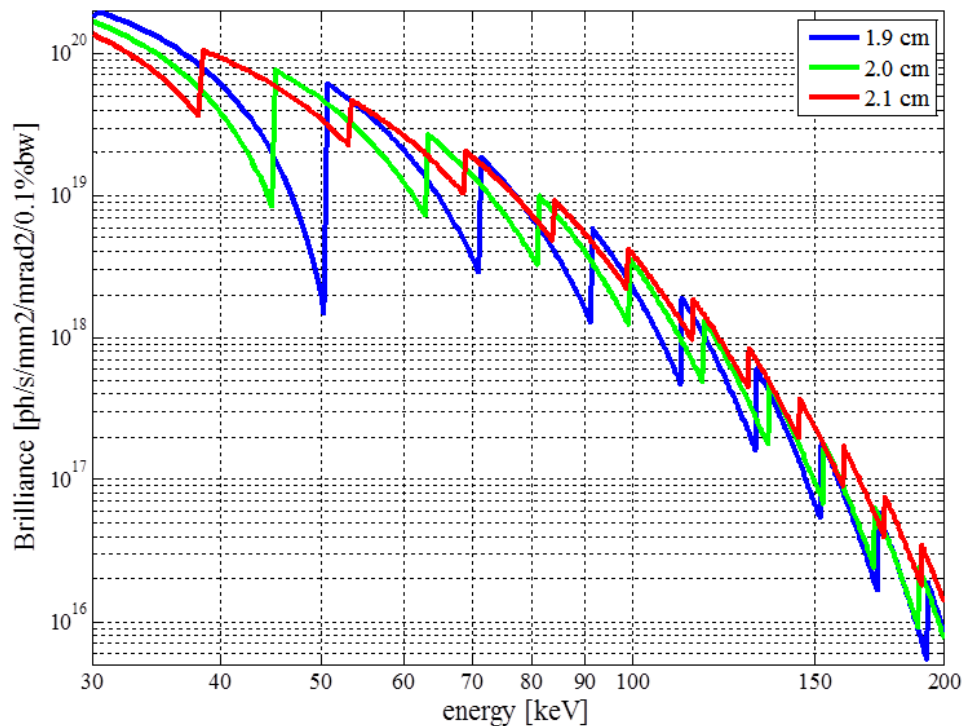

Figure 2.2: Brilliance of a 4 m long in-vacuum undulator for several period lengths.

The total power for the 1.9 cm and 2.1 cm period devices increases from 4.5 kW to 5.4 kW. The 2.1 cm period is preferred since the large jumps between low order harmonics are smoothed out and the improved brilliance at high energies. The increase in total power is tolerable.

The power density distribution at the monochromator of a 2.1 cm period IVU is shown in Figure 2.3. The peak power density is about 20 W/mm^2 and the distribution is significantly wider than the central cone.
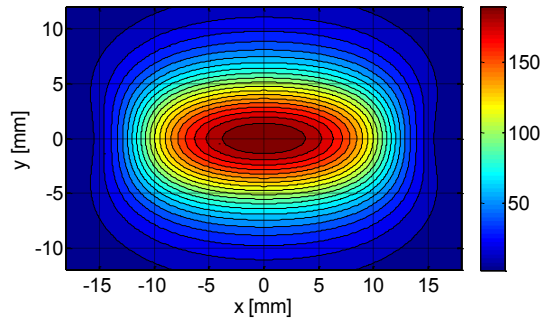
Figure 2.3: Power density distribution of a 2.1 cm period in-vacuum undulator.
The distance from the source is 100 m and units are kW/mrad².

The flux through a 1 mm^2 pinhole at 100 m of a 2.1 cm period in-vacuum undulator (IVU) is shown in Figure 2.4 (left). In the diffraction station at 150 m from the IVU, a flux of about 10^{13} ph/s is predicted at 40 keV through a $1{\times}1$ mm^2 aperture (including efficiency of the optics). The flux decreases with increasing energy by about an order of magnitude per 40 keV. Note that even harmonics from the tenth upward provide flux comparable to the odd harmonics, with the 8th and 6th harmonic only slightly weaker. The widths of the flux distributions for the energies of peak flux are shown in Figure 2.4 (right). Notably, they are significantly wider than the electron beam contribution only which would predict a full width at half maximum (FWHM) of 1.7×0.4 mm^2 (h $\times$ v). Low order even harmonics appear significantly wider horizontally than odd harmonics which is further discussed below.
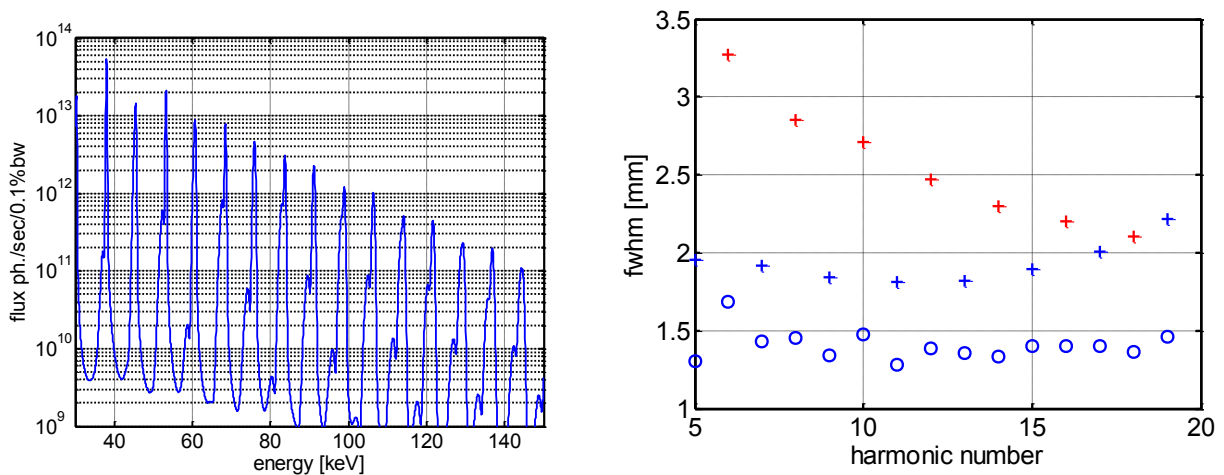

Figure 2.4: Harmonics from a 2.1 cm period in-vacuum undulator at closed gap.
Left: Flux through a 1 mm^2 pinhole at 100 m. Shown are the 5th through 19th harmonic.
Right: Widths (fwhm) of the flux distributions at energies of maximum flux through the 1 mm^2 pinhole at 100 m (circles: vertical, blue plus: odd horizontal, red plus: even horizontal).

Since one of the major methodologies that should be developed at the beamline is "zoom-in" data acquisition, it is crucial that both large beams (several millimeters wide) and micro-focused beams are available. For practical reasons, a vertical rotation axis is much preferable against a horizontal axis and therefore a beam with large horizontal width is beneficial. Since no low-beta option will be available it is worthwhile to investigate the beam profile as function of energy detuning from the peak on-axis brilliance. This is realized at fixed monochromator setting by opening the undulator gap which increases the energy of the

fundamental. Unfortunately, as demonstrated in Figure 2.5, it turns out that odd harmonics (and high order even harmonics) only broaden vertically which is confirmed experimentally by observation of high order harmonics of a U29 undulator at beamline P07.
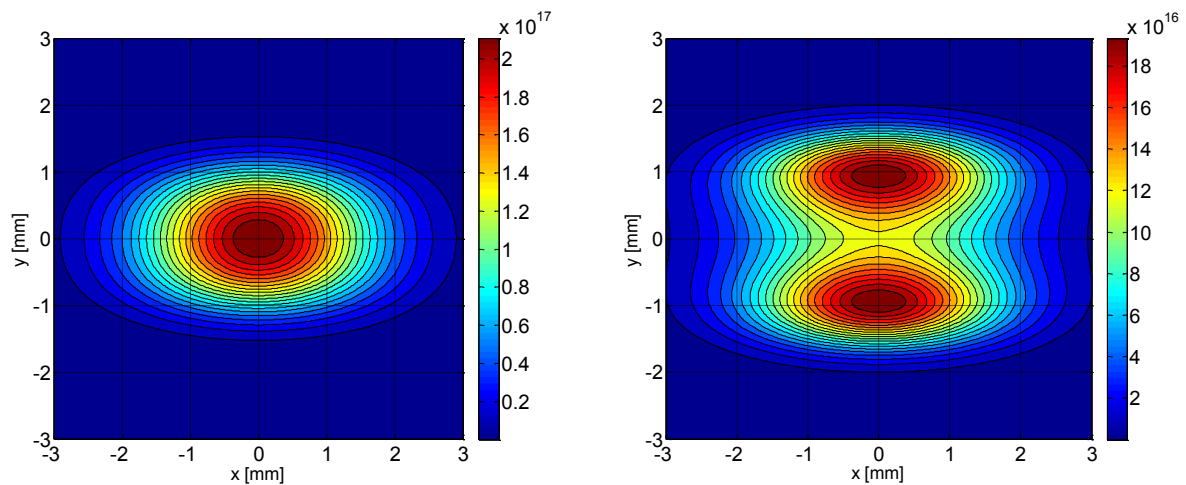

Figure 2.5: IVU flux density of the 7th harmonic for closed gap
at 150 m distance (units in ph./sec/mrad^2/0.1% bw).
Left: A Gaussian distribution is obtained if the monochromator is tuned to the peak energy of 53.32 keV with width (fwhm) of 2.8×1.8 mm^2 (h×v).
Right: Tuning the monochromator 200 eV below this energy increases the vertical but not the horizontal beam width.

However, as shown in Figure 2.6, low order even harmonics should show a significant broadening also in the horizontal direction and the simulated beam width (fwhm) of 6.0×3.6 mm^2 (h × v) in the diffraction station should be sufficient for the intended imaging techniques.
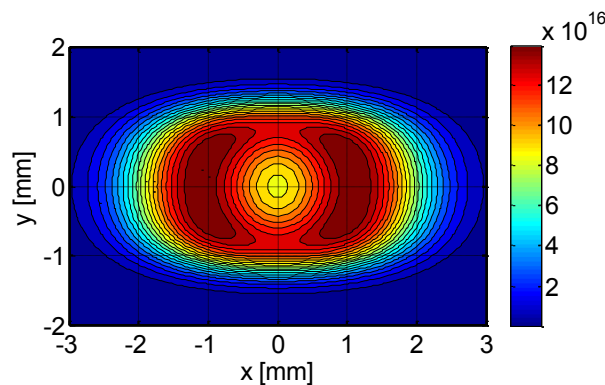

Figure 2.6: IVU flux density of the 6th harmonic for closed gap

at 100 m distance (units in ph./sec/mrad2/0.1% bw). The energy of 45.304 keV is 400 eV below the harmonic. The widths (fwhm, h×v) at 100 m and 150 m are 4.0×2.4 mm^2 and 6.0×3.6 mm², respectively.

2.3 Canted undulator

The canted undulator will be a 2 m device and in-vacuum operation is not foreseen. The smallest period achievable is in this case 23 mm. For energies above 70 keV a device with a

longer period of 29 mm provides more intensity and the spacing between harmonic peaks is smaller, which is advantageous for the operation of the side station with basically fixed energy (see Figure 2.7).
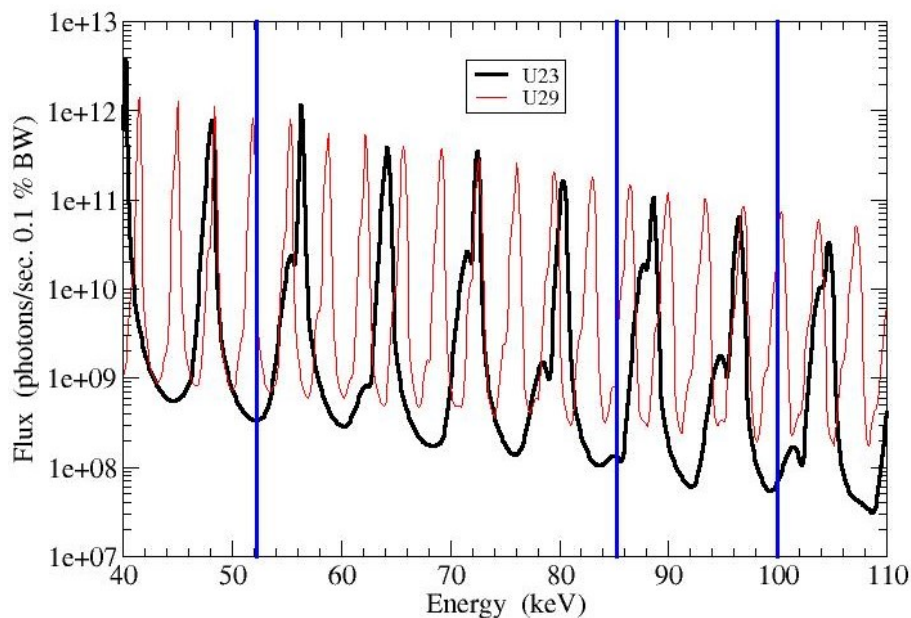

Figure 2.7: Flux from the U23 and U29 undulators

through a 1 mm^2 pinhole at 80 m distance. Blue vertical lines show the side station operation energies.

2.4 Wiggler

The primary function of the wiggler is to provide a large beam enabling tomography on large objects. The proposed beam width is a trade-off between object size, beam handling by the frontend and other optical elements common with the undulator beam, and the total power. A beam width of about 60 mm was considered to be a reasonable compromise. Given a distance of about 120 m from the wiggler to the specimen, an opening angle of ±0.25 mrad is required. Furthermore, high energies up to about 150 keV are required to penetrate cm thick objects. Therefore a wiggler design as compiled in Table 2.2 was proposed by FS-US. Relevant radiation characteristics are shown in Table 2.3, and the beam widths and peak flux are also compiled in Table 2.3 for selected energies. For the EXAFS beamlines at the PETRA III extension a wiggler was dismissed due to undulator like emission structure below the critical energy. Pronounced spatial intensity variations would also compromise the image quality but are not considered a relevant issue since mostly energies well above E_c will be used.

length	2 m
period	4.5 cm
K_{max}	5.6
E_c	32 keV
Total power	8.2 kW
Power within +- 0.25 mrad	5.1 kW

Table 2.2: Wiggler design parameters.

Energy [keV]	50	100	150
hor. fwhm [mm]	96	74	64
vert. fwhm [mm]	13	8.7	7.3
Peak flux per mm^2 [$\times 10^{10}$ ph/s]	36	14	4.6

Table 2.3: Wiggler beam widths and flux at selected energies.
A distance of 120 m is assumed from the source. For the flux a 0.1% bandwidth and no losses in the optics are assumed.
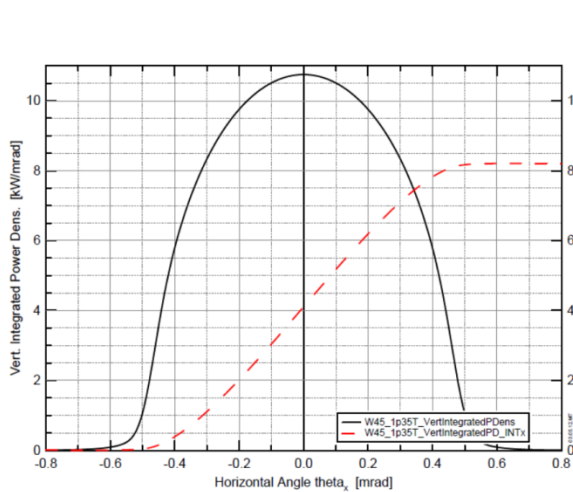

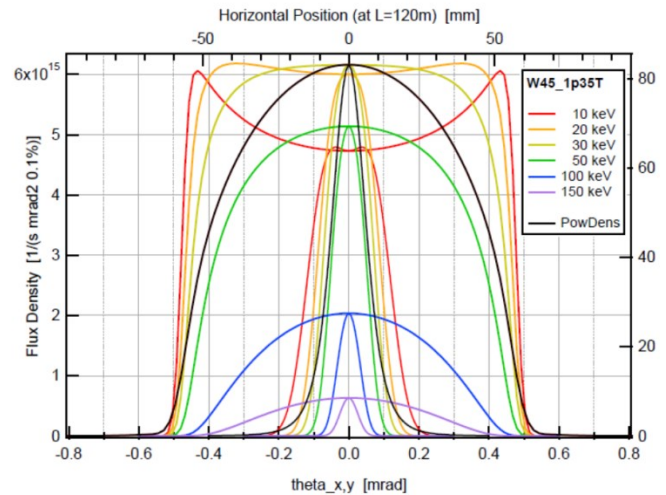Figure 2.8: Vertically integrated wiggler power density.

Figure 2.9: Wiggler flux and power densities.
Energies for flux densities are color coded. Wide and narrow profiles indicate horizontal and vertical distributions, respectively.

2.5 Frontend

Frontend components are provided by the beamline technology group (FS-BT) and are installed within the ring tunnel upstream of the white beam Optics. They include beam filters and a beam monitor, white beam slits and a white beam shutter. A diamond window in OH1 will separate the frontend and OH1 ultra-high vacuum (UHV) vacuum sections. At present, designs for frontend components exist only for an undulator beam and these components will be installed for phase I. The frontend will need to be rebuilt for phases II&III. So far the heat load and beam separation have been considered and it is concluded that they pose demanding constraints but do not endanger technological feasibility. The design of phase II&III frontend components should start as soon as engineering capacity becomes available.

3   High-energy x-ray optics

A brief overview is given of relevant optical elements.

3.1   Crystals

The salient feature of high-energy crystal optics is that Bragg angles are small. Therefore Laue geometry can be exploited and small lattice plane curvatures can result in significant bandwidth broadening since they are compared to the small Bragg angles. While elastic lattice strains also broaden the bandwidth, their effect is typically an order of magnitude smaller than lattice tilts. Furthermore, broadening of the bandwidth is initially accompanied by a steep increase in reflectivity since contrary to the perfect crystal all intensity is directed into the diffracted beam.

Beam divergences can cause significant energy gradients across the monochromatized beam but can be accommodated by crystal bending in meridional and sagittal geometries.

3.1.1   Bent crystals

Geometry

Meridional bending has been the choice for most high-energy monochromators at 3rd generation synchrotron sources and is described by the Rowland circle geometry as sketched in Figure 3.1.
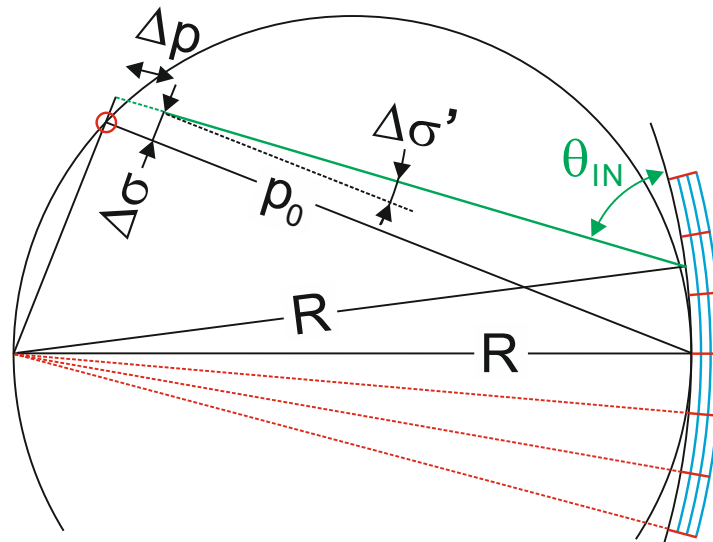

Figure 3.1: Rowland circle geometry.
The divergence from a point source on the Rowland circle (red circle) is compensated by the cylindrical crystal bending with radius R. A ray with phase space parameters [Δσ, Δσ'] is indicated from an extended source moved a distance Δp into the Rowland circle. Δp can be chosen such that energy gradients due to source size and divergence cancel. It is also indicated that symmetric lattice planes (red) do not curve by isotropic bending, whereas planes parallel to the crystal surface (blue) experience the strongest curvature.

The crystal curvature compensates the beam divergence from a point source placed on the Roland circle. It furthermore turns out that energy gradients across the beam can also be mitigated for an extended source if the source is moved slightly inside the Rowland circle.

This is demonstrated by a simple ray-tracing exercise for geometric parameters of the IVU monochromator, the results are shown in Figure 3.2.
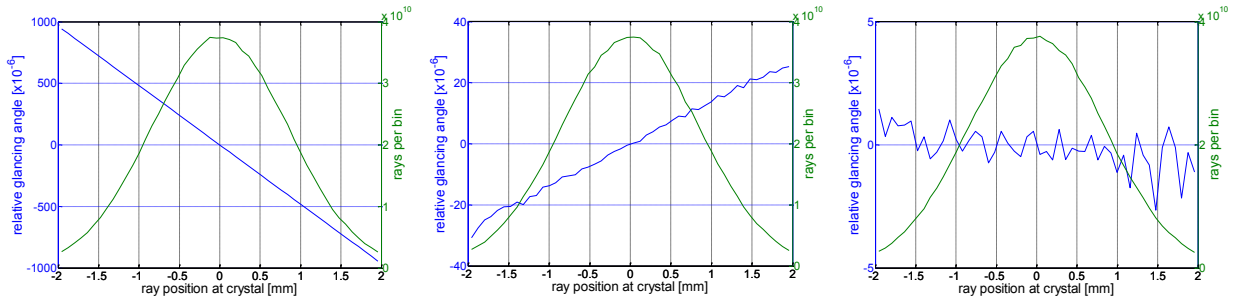

Figure 3.2: Geometric bandwidth in Rowland geometry.
Ray-tracing results at 100 keV for a symmetric Si 111 reflection. Horizontal beam profile (green) at the IVU monochromator and energy gradients across the monochromated beam (blue).
Left: A flat crystal would produce an energy gradient of about 10^{-3} across the about 2 mm wide central cone.
Middle: On Rowland circle this is reduced to 3×10^{-5}.
Right: The energy gradient can be further reduced into the noise of the simulation of about 10^{-6} by moving the source 2.9 m into the Rowland circle.

Sagittal Laue-Laue focusing has recently been demonstrated but is not considered here since (i) a separation of monochromatization and focusing is preferable for "zoom-in" data acquisition, (ii) the bending radii at the high energy end around 150 keV would become alarmingly small, and (iii) the narrow vertical source size would probably not be retained due to the different asymmetric cuts of the crystals. However, sagittal bending is found useful for a symmetric reflection which does not lead to focusing since the bending occurs around the scattering vector. It is found that the anticlastic bending in the meridional plane complies with the Rowland circle geometry and that a desirable bandwidth broadening results for a particular crystal orientation as described in the next section.

Crystal bending and bandwidth broadening

For reflections with large asymmetry, the rocking curve broadening by meridional bending is approximately given by

$$\Delta\theta = \frac{t\cos\chi}{p_0}[(1 - \nu_{21})(\sin\chi\cos\chi) + \tan(\chi)] \tag{3.1}$$

where t is the crystal thickness, χ the angle between the reflecting lattice planes and the crystal surface normal, and p_0 the distance of the crystal from the source (*cf.* Figure 3.1). For a rocking curve width of 50 μrad, which gives $\Delta E/E = 10^{-3}$ for Si 111 at 40 keV, a typical asymmetry angle of $\chi = 35.3°$, p_0 equal to 100 m, and an average Poisson ratio $\nu_{21} = -0.25$, the crystal thickness is calculated as 4.7 mm and the x-ray path length would be 5.8 mm.

For isotropic crystals no rocking curve broadening results from bending for symmetric reflections since bending and lattice strain contributions cancel (the lattice planes remain

flat). It is also known that broadening of symmetric reflections can arise for elastically anisotropic crystals and this is briefly described for the relevant case of sagittal mediated meridional bending. The geometry is shown in Figure 3.3, the sagittal bending around the y-axis causes anticlastic bending around the z-axis. At the center of the crystal, this is described by the following equation:

$$
\varepsilon_i = s_{ij}\sigma_j =
\begin{bmatrix}
5.91 & -0.958 & -1.55 & 0 & 0 & -1.67 \\
-0.958 & 5.32 & -0.958 & 0 & 0 & 0 \\
-1.55 & -0.958 & 5.91 & 0 & 0 & 1.67 \\
0 & 0 & 0 & 17.3 & 3.34 & 0 \\
0 & 0 & 0 & 3.34 & 14.9 & 0 \\
-1.67 & 0 & 1.67 & 0 & 0 & 17.3
\end{bmatrix}
\begin{bmatrix}
0 \\
\sigma_{yy} \\
\sigma_{zz} \\
0 \\
0 \\
0
\end{bmatrix}
=
\begin{bmatrix}
\sigma_{yy}s_{12} + \sigma_{zz}s_{13} \\
\sigma_{yy}s_{22} + \sigma_{zz}s_{23} \\
\sigma_{yy}s_{23} + \sigma_{zz}s_{33} \\
0 \\
0 \\
\sigma_{zz}s_{36}
\end{bmatrix}
=
\begin{bmatrix}
\sigma_{yy}s_{12} + \sigma_{zz}s_{13} \\
t/2R_z \\
t/2R_y \\
0 \\
0 \\
\Delta\theta/2
\end{bmatrix}
\quad (3.2)
$$

where the compliances are given in TPa^{-1} and are calculated for a Si crystal orientation as shown in Figure 3.4 ([111] || y, [1-10] || z). σ_{zz} is the stress in z-direction at the crystal surface due to the applied bending moment, σ_{yy} is a stress that counteracts the anticlastic bending to reduce the total elastic energy. t is the crystal thickness and R_y and R_z are the sagittal and meridional bending radii, respectively. Note that there is a shear strain (but no shear stress) in the xy plane, $\sigma_{zz}s_{36}$, which is equal to half the width of the resulting broadening of the [111] reflection. Also note that the other shear strains are zero preventing the crystal from twisting. The plane stress model was tested against FEM simulations. σ_{yy} has to be taken from the FEM simulation but σ_{zz} and all strains are then found to be in excellent agreement.
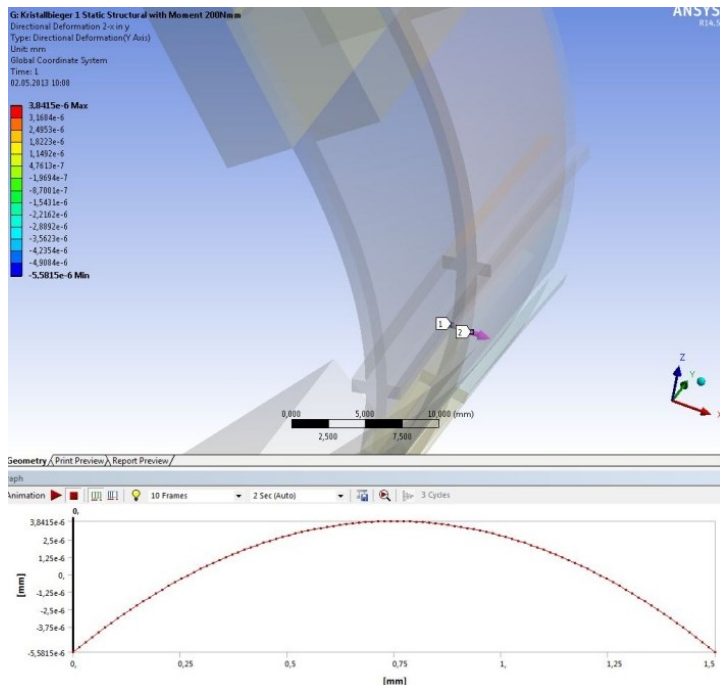

Figure 3.3: FEM simulation of IVU monochromator crystal.
The curvature of the diffracting lattice planes is demonstrated in symmetric Laue geometry by sagittal mediated meridional bending.
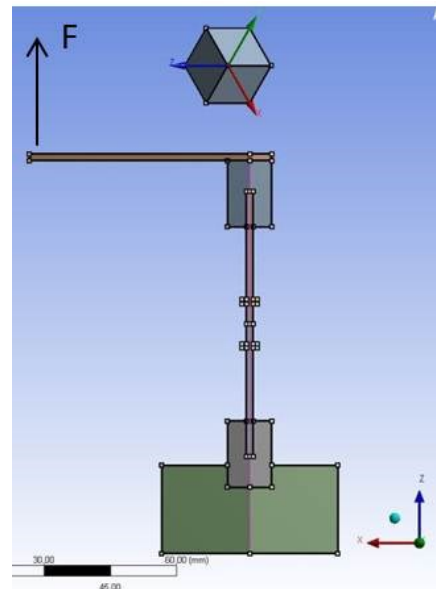

Figure 3.4: Crystal orientation and geometry of leaf-spring moment bending.
The bending force F is indicated.

Present simulations on a 1.5 mm thick crystal and a sagittal bending radius of 9.3 m predict a rocking curve width of 47.1 μrad and meridional bending radius of 100.3 m. The FEM

simulations predict a systematic dependence of the sagittal bending radius that is required for a 100 m meridional bending radius as function of the height-to-width ratio of the crystal. Compared to meridional bending, the same rocking curve width can be obtained by an about four times shorter path length in the crystal. At 40 keV, the transmission through two crystals of the considered crystal thicknesses is about four times higher for the sagittal than for the meridional bending.

3.1.2 Si-Ge gradient crystals

Another way to increase the width of the rocking curve is the use of a Si-Ge crystal (Keitel *et al.*, 1998). A curvature of the lattice planes is achieved by growing a Ge concentration gradient into a Si crystal. The curved lattice gives rise to a high reflectivity above 90 % in the Laue case and tunable large rocking width which depends on the concentration gradient and the crystal thickness, ranging from a few ten μrad to about one mrad. The corresponding bandwidths are in the range of 0.01 to 1 %. The crystal thickness is 7 mm in this case.

The disadvantage of these types of crystals is that the rocking curve width depends on the Ge gradient grown into the Si lattice which, depending on the crystal quality, can be rather inhomogeneous and the gradient direction is limited to the [111]-direction due to growth restrictions. Consequently a Si-Ge gradient crystal is less efficient for a (311) reflection.

3.1.3 Temperature gradient crystals

A similar curvature of the lattice of a Si crystal can be obtained by a temperature gradient dT applied parallel to the scattering vector of the crystal. The bending radius of the lattice is given by R = h/(α * dT) where α is the thermal expansion coefficient and h the width of the crystal in the direction of the temperature gradient. For a crystal with a length l along the beam the rocking curve width is

$$FWHM = \frac{l}{h}\,\alpha\,dT. \tag{3.3}$$

Furthermore, the reflectivity is expressed as

$$\frac{I}{I_0} = 1 - \exp(-\frac{\pi^2}{4}\frac{l\cdot\delta}{d\cdot FWHM}) \tag{3.4}$$

with Darwin width δ and extinction length d (Rütt *et al.*, 2010). The rocking curve dependent reflectivity for Si(111) and Si(311) reflections are plotted in Figure 3.6. With these crystals used as a monochromator for high energy x-rays a tunable bandwidth between 0.01 and 1 % can be obtained. However, relatively thick crystals have to be used to achieve a large bandwidth, e.g. for a Si(311) crystal with a thickness of 5 mm a bandwidth of 0.1 % has been achieved at 100 keV.
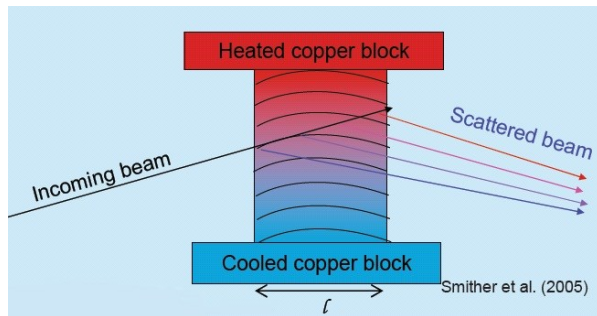
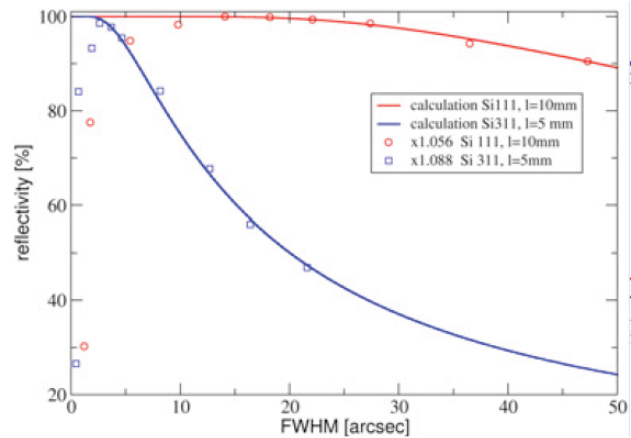**Figure 3.5: Schematics of a temperature gradient monochromator.**

Figure 3.6: Gradient crystal reflectivities.
Measured and calculated reflectivities at 100 keV of a thermal gradient crystal monochromator for Si(111) and Si(311) reflections.

3.2 Multilayers

The versatility of multilayers as x-ray optical elements arises from the ability to realize both depth and lateral d-spacing gradients. At high energies small d-spacings are desirable to prevent excessively long footprints and increase beam coverage. The smallest d-spacing is constrained by interface roughness through a Debye-Waller factor like dependency of the reflectivity. The effective roughness depends on the roughness of the substrate and the intrinsic interface quality. Typically 2-3 Å are achieved which translates into a Debye-Waller factor limited reflectivity of about 70% for a d-spacing of 25 Å. The reflectivity of a W/B_4C multilayer with a 25 Å period at 68.5 keV has been reported as 75% (Lienert et al. 1998).

Even smaller roughness values are reported for favorable material combinations and advanced deposition methods, but commercial availability for high-energy relevant systems is uncertain. The bandwidth of periodic high contrast multilayer coatings is typically around 1% and dominated by extinction. Larger bandwidths can be obtained on cost of reflectivity by varying the d-spacing across the depth of the coating. This is particularly efficient at high-energies due to their large penetration power. It is significant to note that W which forms excellent interfaces with Si and B_4C has it's K-edge at 69.5 keV, right in the middle of an interesting energy range for diffraction. W based depth graded multilayers would therefore display poor reflectivity above the W K-edge. Reports on the performance of non W multilayer coatings at high-energies are rare.
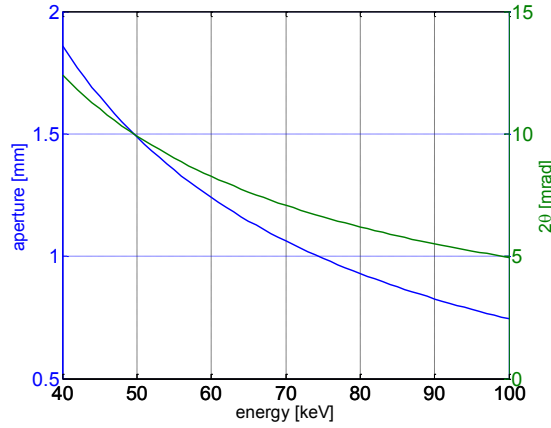
Figure 3.7: Multilayer aperture and scattering angle as function of the x-ray energy for a length of 300 mm and a d-spacing of 25 Å.

The focusing geometry is given by an ellipse and the glancing angle θ changes along the footprint as described up to second order by (Lienert et al. 1999)

$$\frac{\Delta\theta}{\theta}(\Delta x) = \frac{1}{2}\left(\frac{1}{q} - \frac{1}{p}\right)\Delta x + \frac{3p^2 - 2pq + 3q^2}{8(pq)^2}\Delta x^2 \tag{3.5}$$

where p and q are the source-to-multilayer and multilayer-to-focus distances, respectively, and Δx measures along the beam footprint from the center position given by p and q. The bending radius at p and q is given by

$$\frac{1}{R} = \theta_{ML}\frac{p+q}{2pq} \tag{3.6}$$

The changing glancing angle can be compensated by a lateral d-spacing gradient according to equation (3.5). Thus, the focal length q is confined by the lateral gradient but changes in energy can be accommodated by appropriate shape adjustment which suggests a dynamical bending mechanism. The achievable focus size critically depends on the slope error, σ_{rms}, of the shaped multilayer and can be estimated as $2 \times 2.36 \times \sigma_{rms} \times q$.

Finally, typical parameters and constraints are discussed. At high energies divergences dominate the reciprocal space resolution due to the small Bragg-angles and 1 mrad may be considered as an upper limit. In order to exploit the large aperture in the mm-range, the focal length should be at least 1 m. For a 300 mm long multilayer the d-spacing gradient would be about 15% which should not present technological problems. A rms slope error of 1 μrad would cause a spreading of the diffracted rays of 2 μrad which is comparable to the apparent horizontal source divergence (source size divided by the source-to-optics distance) but about 25 times larger than the apparent vertical source divergence. Thus, emittance conserving source imaging is only possible in the horizontal plane. However, it is noted that the apparent source divergence can be increased by beam collimation with CRLs. A 1 μrad rms slope error would cause a FWHM broadening of the focal spot of about 5 μm per meter focal length.

3.3 Compound refractive lenses

Compound refractive lenses (CRL) are an array of individual lenses to collimate or focus x-rays. The focal length is given by $f = R/2\delta N$ with the radius of curvature R and δ the difference of the refractive index from one (Figure 3.8). N is the number of lenses. Since the refractive index depends on energy, CRL's are chromatic devices. Furthermore, the lens is described by the effective aperture D_{eff}, which is the geometric aperture convoluted with absorption and is given by

$$D_{eff} = 4 \, (f \, \delta \, L)^{\,1/2} \tag{3.5}$$

where L is the attenuation length of the lens material (Lengeler *et al*. 1999). One should note that D_{eff} does not consider the thickness d of the lens.
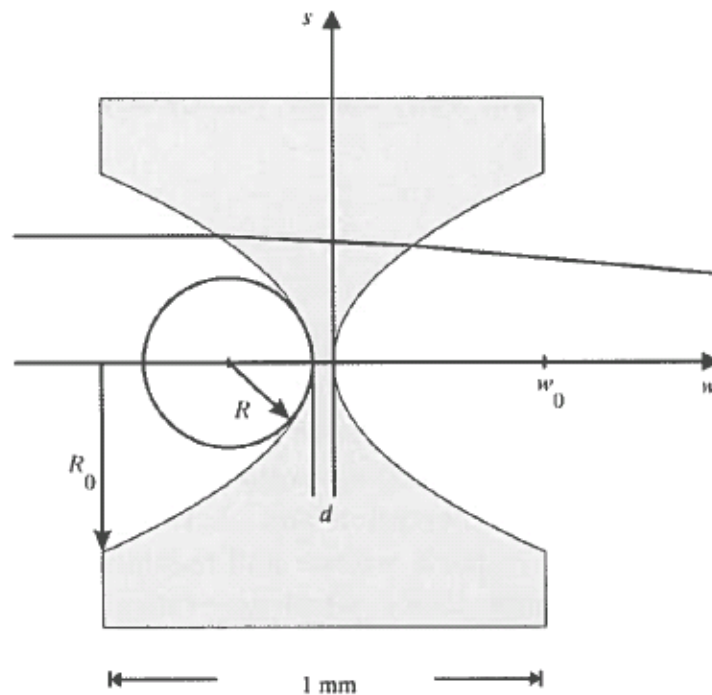

Figure 3.8: Parabolic compound refractive lens with radius R.
 (Lengeler 1999)

The refraction of a CRL is based on the absorption of the lens material. Thus the material needs to be adapted to the x-ray energy with δ/μ maximized. Compton scattered photons do not contribute to the intensity in the focal spot. Consequently, in the high energy x-ray regime elements like Al and Ni are more favorable for lens material than e.g. Be that is used in the conventional x-ray regime.

Commercially available CRL's usually have a parabolic shape pressed into Be, Al or Ni. They are available in spherical symmetric geometries for horizontal and vertical focusing or as linear devices for focusing only a single direction, e.g. for non source size conserving monochromator optics the direction that is not affected by the monochromator. More recently, devices manufactured by the LIGA technique became available. This allows the production of high aspect ratio shapes of a few millimeters with surface roughness in the range of 10 nm.

Calculation of optimum lens parameter can be performed with the program crlcalc at the website of RWTH Aachen.

Figure 3.9 and Figure 3.10 show the number of lenses and effective aperture as a function of focal length for different lens radii and energies between 40 and 200 keV for Al and Ni, respectively.

More recently a kinoform lens has been exploited for focusing of x-rays, which is a combination of a CRL with a zone plate. This device overcomes the limited effective aperture of a parabolic CRL. The use for high energy x-rays needs to be demonstrated. Other focusing devices known from conventional x-ray energies like e.g. zone plates and capillaries are less efficient in the high energy x-ray regime.
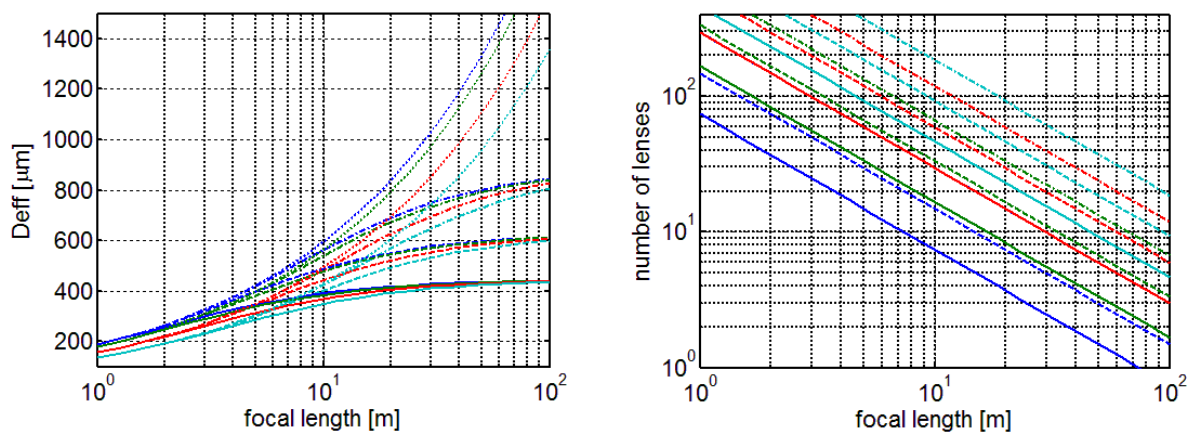

Figure 3.9: Properties of Al CRLs as function of focal length.
Energies are color coded as blue 40 keV, green 60 keV, red 80 keV, and cyan 100 keV. Lens radii (R | 2R0) are line style coded as solid: 50 µm | 447 µm, dashed: 100 µm | 632 µm, dash doted: 200 µm | 894 µm. Left: Effective aperture, the dotted lines are the envelopes for infinite R0 as given by equation 3.5. Right: Number of lenses.

Figure 3.10: Properties of Ni CRLs as function of focal length.
Energies are color coded as blue 100 keV, green 130 keV, red 160 keV, and cyan 200 keV. Lens radii (R | 2R0) are line style coded as solid: 50 µm | 447 µm, dashed: 100 µm | 632 µm, dash doted: 200 µm | 894 µm. Left: Effective aperture, the dotted lines are the envelopes for infinite R0 as given by equation 3.5. Right: Number of lenses.
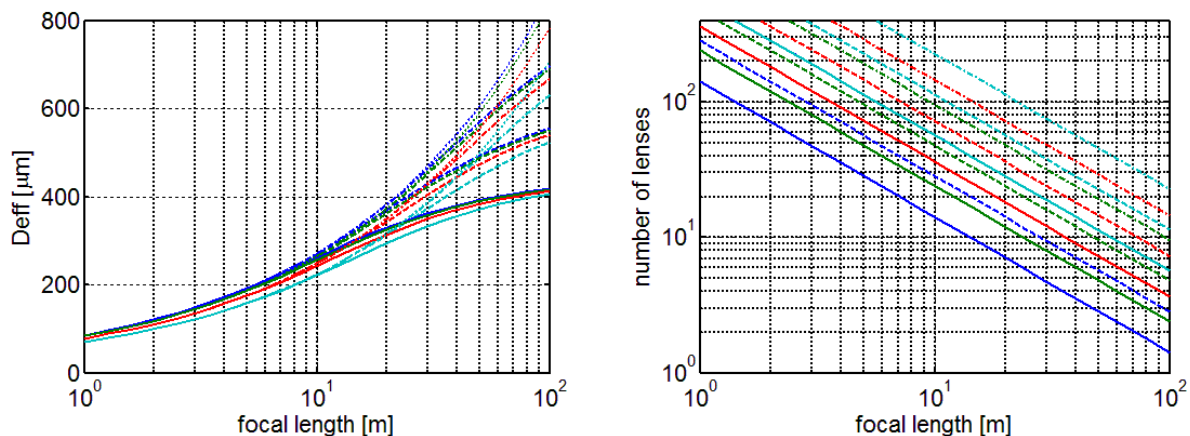
4   Detectors

While the penetration power of high-energy x-rays enables the exploration of diffraction from bulk materials through complex sample environments, it also impedes an efficient detection in particular at high spatial resolution. It is also noted that many high-energy diffraction applications are detector limited and detector performance will therefore be crucial. A brief overview of existing and developing detectors is given. For diffraction the most important parameters are the number and size of pixels, dynamic range, and frame rate. It will become clear that complementary detectors are required even for individual techniques.

4.1   Large area detectors

Flat panel large area detectors are extremely powerful tools for high-energy diffraction since a large amount of reciprocal space is condensed with little distortion. As far as reciprocal space resolution is concerned, large pixel sizes can be compensated by increasing the distance to the sample which increases the measurement sensitivity of scattering angles but decreases information on the location of scattering events.

Good efficiency is obtained at pixel sizes of about 200 μm since even K-fluorescence from the detection material is efficiently collected. Disregarding storage phosphor image plates due to their slow point-by-point readout, and Selenium flat panel detectors due to persistent performance issues, the remaining available systems convert x-rays to visible light by a phosphor screen. Detectors developed for medical imaging use CsI needle structured scintillators and provide good efficiency but a typical dynamical range below 12 bit. Furthermore, factory provided distortion and flat-field corrections are geared towards imaging applications and are often unsatisfactory for diffraction applications.

Amorphous Si based flat panel detectors are commercially available from several companies. Two detectors that have performed satisfactory at synchrotrons are the Perkin Elmer XRD 1621 (PE1621) and General Electric Revolution 41RT (GE41RT). Selected parameters are compiled in Table 4.1.

Intrinsic to the use of amorphous Si is an image lag of typically few percent of the primary exposure. The image lag depends in a non-linear way on the primary exposure intensity. It is also noted that continuous read out of the amorphous Si detectors is enforced by the controller to prevent charge build up from dark current. Enforced reading during idle periods poses a problem for deterministic response to external trigger events. Finally, the point spread is only slightly larger than one pixel such that an accurate peak center fitting can be difficult for sharp diffraction peaks.

The distance between the active area and the physical edges of the detector are relative small for the GE41RT but at least 10 cm for the PE1621. Therefore combining several PE1621 to a matrix detector would leave significant dead areas. Finally it is noted that at present the GE41RT frames are first accumulated in memory while the PE1621 images can be streamed to disk.

	GE41RT a-Si	PE1621 a-Si	PE2923 CMOS
CsI thickness [μm]	500	500	600
Number of pixels	2048 × 2048	2048 × 2048	3888 × 3072
Pixel size [μm]	200	200	74.8
Area [cm^2]	41.0 × 41.0	41.0 × 41.0	29.1 × 23.0
Frame rate unbinned [Hz]	8	15	26
Frame rate binned 2x2 [Hz]		30	70

Table 4.1: Selected performance parameters of flat panel detectors.

Recently large area CMOS detectors have become available (PE2923) by combining four smaller modules. The PE1621 and an individual CMOS module (PE1512) have been tested at the P07 beamline. A comparison of selected parameters is compiled in Table 4.1. Most remarkably, the CMOS detector showed no significant image lag for exposures below the saturation level. Also, the active area of the PE2923 is as close as 3 mm to a long edge of the housing suggesting that two modules can be combined to a matrix detector. On the other hand, the CMOS detector has one pixel spacing between the modules and reduced sensitivity for some rows that are partially covered by signal lines. Furthermore, the CMOS detector requires a lead loaded fiber plate between the CsI scintillator and CMOS chip which causes some signal degradation. However, in terms of performance parameters a matrix of two PE2523 CMOS detectors is considered superior to a PE1621 a-Si detector.

Before the advent of large pixel detector arrays, CCD arrays have dominated the crystallographic applications due to their superior dynamic range. By optimized parallel readout frame rates of 2.5 Hz are reported for 15 Mpixel images. CCD arrays with efficient phosphors at high energies would be of interest since high-Z pixel detector modules will most likely be significantly more expensive than the existing Si modules and coverage of a large area might not be affordable. While CCD arrays with high-energy efficient phosphors are not commercially available at present, this could change in the near future.

4.2 Medium area detectors

Smaller pixel sizes are required either for increasing the reciprocal space resolution at fixed detector-to-sample distance or for increasing sensitivity to the spatial origin of diffraction events.

Integrating detectors

In integrating detectors better spatial resolution is usually obtained by thinner phosphor screens which sacrifices efficiency. Efficiency losses can be dramatic when secondary events such as x-ray fluorescence become likely to escape. The resolution of thick phosphor screens can to some extend be improved by micro-structuring such that at least the spread of the visible light is confined. Needle grown CsI scintillators are one example but the achievable needle diameter limits the resolution. Phosphor screens based on a filled micro-structured Si matrix are commercially available (Scint-X) but the choice of commercial detectors equipped with the structured scintillators is still rather limited.

Pixel detectors

High energy pixel detectors are semiconductor based pixelated single photon counters. This has the advantage of a relatively high efficiency, which depends on the thickness of the semiconductor, and low noise, since photons are not converted into light, but counted directly. This technology enables photon energy resolution and allows to remove e.g. fluorescence background. While Si-based devices for energies below 20 keV are on the market since a few years, high energy devices based on Germanium or Cadmium-Telluride are in the development phase. A CdTe prototype based on a medipix chip with 256 x 256 pixels and a pixel size of 55 x 55 μm has been tested at beamline BW5 and was found to be very efficient for the determination of small and diffuse scattering signals, despite the fact that the CdTe sensor had a few dead spots and pixels.

4.3   Imaging detectors

High-energy imaging detectors are based on the conversion of x-rays to visible light in thin single crystal scintillators and magnified imaging (often including a deflecting mirror) onto a CCD or CMOS camera. The hallmark features are low efficiency on the percent level and geometric constraints that require custom designs. Particularly desirable features are (i) the possibility to position the scintillator as close as few millimeters from a specimen in a load frame, (ii) semi-transparent design such that a far-field detector can be operated simultaneously, (iii) simultaneous operation of two near-field screens with few mm distance, and (iv) 16 Mpixel or larger detectors. Detectors with the listed individual features have been designed but a combination of features has proven difficult to achieve.

The conversion of x-rays to visible light fundamentally limits the resolution to about its wavelength. Furthermore, the thickness of the scintillator is restricted to the depth of focus of the imaging optics (typically microscope objectives) and the scintillator should be free standing to avoid smearing of the energy deposition by scattering from a substrate. Even then test experiments indicate that the resolution limit set by the visible light optics is not reached at high-energy x-rays pointing towards a significant spread in the energy deposition. Micro-structured scintillators have been developed that would overcome the thickness constraint by the depth of focus of the visible light optics but the achievement of micrometer pitches has proven to be difficult.

In conclusion, the conversion of the high-energy x-rays to visible light inherently limits the resolution to about 1 μm at best and precludes efficient detection. The actual resolution and efficiency tend to improve with decreasing energy. Still, significant progress can be achieved by optimized opto-mechanical designs to accommodate the above listed features.

4.4   Point detectors

Ionization chambers and diodes are used to measure the incoming flux on the sample. At high energies ionization chambers are filled with N_2 or heavy inert gases e.g. Argon and give an efficiency between a few tenth and a few percent. In combination with controlled gas pressure and low noise current amplifiers ionization chambers allow also a quantitative determination of the photon flux. Furthermore, with special geometry they can be used to determine the beam position.

Similar to ionization chambers, diodes convert photon flux into current by absorbing part of the x-ray beam. Si PIN diodes and PIPS diodes are used. No energy resolution is obtained. By using avalanche photo diodes (APD) time resolution on the order of 1 ns can be obtained. However, due the small thickness between 10 and 100 µm their sensitivity for high energy x-rays is limited.

Scintillation counters are single photon counters which provide photon energy resolution by analyzing the pulse height by a multichannel analyzer. Depending on the thickness of the CsI scintillator, efficiencies close to 90 % can be achieved. The energy resolution is in the range of 10 %. Since the detector electronics are based on electron avalanche it is not suited for measurements in magnetic fields.

Solid state detectors (SSD) are semiconductor based single photon counters which achieve highest energy resolution. For high energy x-rays the semiconductor material can be either Germanium (Ge) or Cadmium-Telluride (CdTe). While Ge can be obtained in any size and thus adapted to the measurement problem, CdTe is only available in small size with a maximum lateral size of 5 x 5 mm^2 and thickness of 0.5 mm, limiting the efficiency at 100 keV to 60 %. However, CdTe-detectors are very compact since Peltier cooling is sufficient. In contrast Ge has to be cooled to liquid nitrogen temperature, which requires either a large Dewar or an electric cooling device like a pulsed tube cooler. The energy resolution of both Ge and CdTe detectors is in the range of 0.5 %. In combination with fast digital amplifiers count rates of about 10^6 counts/sec. can be achieved for both Ge and CdTe detectors.

5   P21.A In-line branch: diffraction & imaging

5.1   White beam optics (OH1)

The in-line and side branches of P21 share the white beam and monochromatic beam optics hutches, OH1 and OH2, respectively. OH1 will accommodate monochromators for the side station, for the in-line IVU, and wiggler. Because of the very different radiation properties of the wiggler and the IVU two separate monochromators are required. To avoid compounding complexity, it is suggested to separate the functionalities into two separate vacuum tanks.

A top view of the white beam optics hutch is shown in Figure 5.1.

Figure 5.1: Top view of the OH1 (red border) and OH2 (yellow border) hutches. No optics components are shown in OH2.

5.1.1   In-vacuum undulator monochromator

The monochromator should deliver the following beam conditioning:

(i)   Energy range of at least 40 to 150 keV in fixed exit geometry.

(ii)   Retain the beam emittance.

(iii)   Transmit a relative energy bandwidth of $1\text{-}2\times10^{-3}$ with good efficiency. This bandwidth roughly matches the ratio of the point spread divided by the diameter of area detectors. It is also in the range of typical peak broadening due to microstrains or moderate size broadening.

(iv)   Confine the relative energy gradient over the central cone within 10^{-4} or better. This is required for accurate strain measurements.

(v)   Provide a large beam (unfocussed central cone) for imaging and diffraction imaging applications ("zoom-in" data acquisition). Focusing will be achieved by separate optical elements, most likely CRLs and possibly curved multilayers.

(vi)   Not interfere with the wiggler beam when used.

A double bounce monochromator is required and for reasons (v), (ii), and (i) the recently demonstrated sagittal Laue focusing geometry (Zhong *et al.,* 2001) is ruled out. Only Si 111 reflections are considered.

Flat crystals vs. Rowland geometry

A horizontal diffraction plane is chosen for two reasons. First, even the apparent source divergence (σ_{FWHM} = 3.3 μrad, source size divided by the distance to the monochromator) in the horizontal plane is significantly smaller than the bandwidth limited angular acceptance of the monochromator (even at 200 keV: $\theta_{111}/1000$ = 10 μrad). This is required for good efficiency of the monochromator. Second, the apparent source divergence in the vertical plane is extraordinary small (0.15 μrad) such that it could not be retained by a vertical scattering plane (while it potentially could be exploited by micro-focusing).

The geometry of a Laue-Laue monochromator in Rowland geometry is sketched in Figure 5.2. Note that the non-dispersive arrangement of two similar reflections significantly reduces the polychromatic divergence from a single reflection. Rowland bending is preferred against a flat crystal since the latter produces a significant energy gradient across the central cone as shown in Figure 3.2.
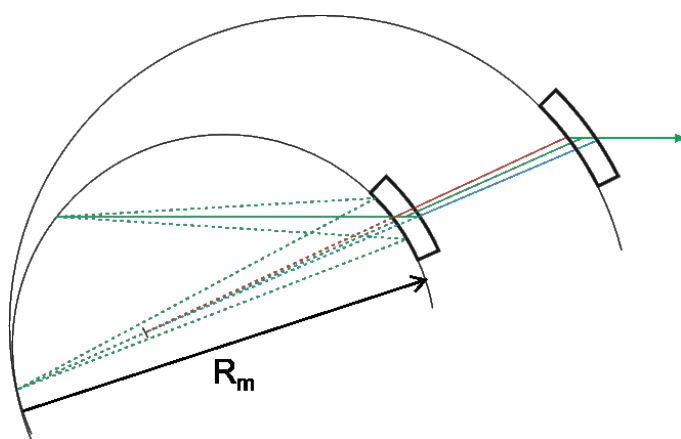

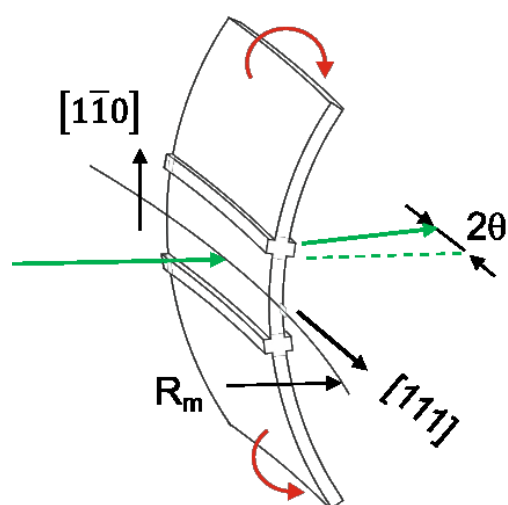**Figure 5.2: Geometry of a Laue-Laue double crystal monochromator.**

Figure 5.3: Shaping of the IVU monochromator crystal by sagittal mediated meridional bending.

The preference of Rowland bending is another consequence of the large source-to-monochromator distance since the beamsize at the monochromator is dominated by the beam divergence rather than by the source size. Furthermore, bending provides the possibility to also mitigate the minor energy gradient across the beam due to the finite source size by slightly moving the source inside the Rowland circle, which is relevant for d-spacing measurements on polycrystals.

Crystal bending

Existing high-energy Laue-Laue Rowland monochromators at PETRA III, the ESRF and the APS are positioned about 30 m from the source and employ meridional bending. By appropriate asymmetric cuts and crystal thicknesses, a bandwidth $\Delta E/E$ of about 10^{-3} is obtained from a path length of the x-ray beam within the Si crystal of 2-3 mm. Since the source to monochromator distance at P21 is around 100 m and the Rowland circle radius increases accordingly, the same bandwidth would require about three times thicker crystals and a path length of about 5.8 mm per crystal (*cf.* section 3.1.1). The total transmission at 40 keV would be 16%.

As described in section 3.1.1, a bandwidth $\Delta E/E$ of 0.1% can be achieved at 40 keV in sagittal mediated bending to a meridional radius of 100 m from a path length of about 1.5 mm. The total transmission at 40 keV is about 62% and the absorbed heat is reduced. In the symmetric case proposed here, the sagittal bending occurs exactly around the scattering vector and should therefore not change the diffraction geometry. Furthermore, since the primary bending axis is perpendicular to the diffracting lattice planes, vibrations around this axis should be invisible to the x-ray beam. The geometry also has the convenient features that bending, to first order, does not change the glancing angle and that the Rowland circle radius is essentially independent of the selected energy.

For the above listed reasons sagittal mediated bending is the favored option. On the other hand, the fact that the sagittal bending controls both the bandwidth and meridional bending requires that any spurious meridional bending should be significantly smaller than the about 100 m Rowland circle bending. This requires careful control of the crystal clamping and temperature gradients across the crystal thickness. The bending strain is 1.5mm/100m = 15×10^{-6}. At room temperature where the expansion coefficient of Si is about 2.5×10^{-6} 1/K, the same bending would be caused by a cross-thickness temperature gradient of 6 K. As presented in the following section, the heat load problem is greatly reduced by cryogenic cooling.

Meridional bending is the fall back option. Due to the significantly increased beam path in the monochromator crystals, the lower energy would be above 40 keV and the bandwidth would need to be reduced.

Heat load and cooling

Cryogenic cooling is motivated by a zero transition of the thermal expansion of Si at 120 K (with a slope of about 1.7×10^{-8} K^{-2}) and an about five times improved thermal conductivity. On the other hand, it tends to introduce significant vibrations and requires UHV environment to prevent "icing" of the cold components.

The total power of the IVU through a 1 mm^2 aperture at 100 m is about 20 W. At high energies the absorbed power in a Laue crystal can be reduced significantly by beam filtering. At PETRA III diamond filters are available coated with a total of 50 μm Cu. The spectral transmission through cumulative Cu filters is shown in Figure 5.4.
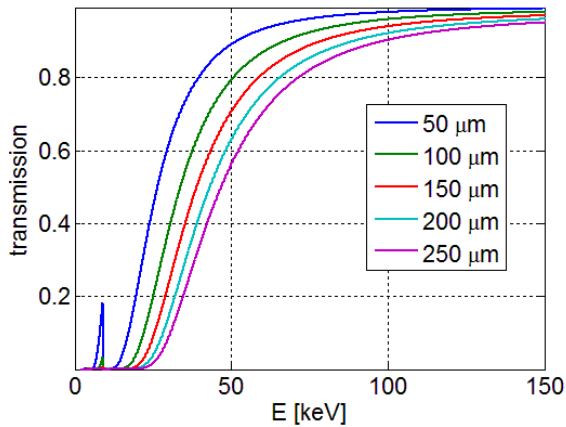
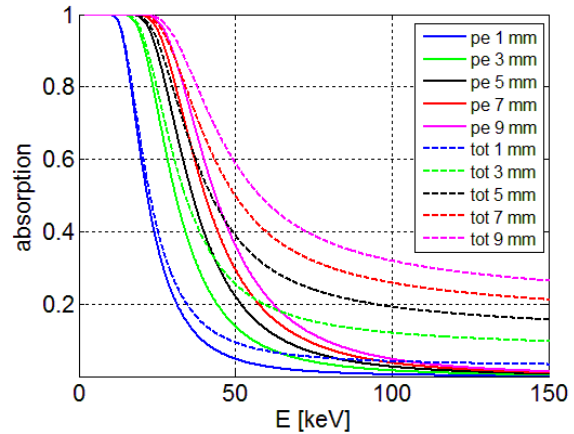**Figure 5.4: Spectral transmission through cumulative Cu filters.**

Figure 5.5: Absorption for various path lengths in Si.
The attenuation is plotted for photoelectric only and photoelectric and scatter interaction.

At 40 keV the transmission through 100 μm Cu is 65% and the transmitted total power per mm² is 7.7 W. Due to beam hardening, the photoelectric absorption in a subsequent Si crystal is rather small (see Figure 5.5) such that only a power P of 1 W is deposited in a 1.5 mm thick Si crystal under normal incidence per mm². The depth dependent power deposition (sum of the kinetic energies of all primary charged particles released by an interacting photon) is shown in Figure 5.6.
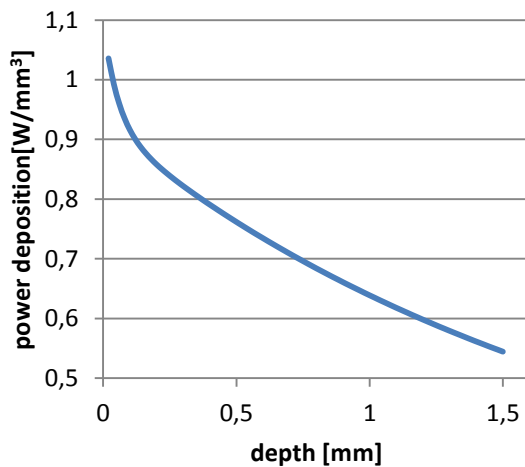

Figure 5.6: Depth dependent power deposition in Si. The spectral flux density from the 21 mm IVU was hardened by a 100 mm Cu filter.

For a simulation of heat load effects an incident beam size of 4.0×2.4 mm² is assumed, covering the central cone of the 6th harmonic (c.f. Figure 2.6). The total power deposited in a 1.5 mm thick crystal under normal incidence is about 10 W. FEM simulations have been performed for a depth dependent power deposition as described above and a temperature dependent expansion coefficient. A monolithic crystal design was considered with a central plate geometry (40×29×1.5 mm³) and wider basis (5×29×20 mm³). The dimensions are derived from an FEM optimization of the width-to-height ratio of the crystal and minimizing parasitic mounting strains.

Therefore only 5 mm wide stripes of the bottom side of the lower basis are in contact with the cooled mounting plate and this geometry was implemented for the FEM simulations. The temperature on the front side of the crystal is shown in Figure 5.7. The temperature difference between the illuminated volume and the cooled base is about 10 K. This is in good agreement with a simple estimation assuming heat flow to one cooled edge of the crystal a distance h from the beam, a crystal width w and thickness t. The temperature difference ΔT from the beam to the edge is estimated as

$$\Delta T = - \frac{P \cdot h}{t \cdot w \cdot \lambda} \qquad\qquad (5.1)$$

For crystal dimensions (h = 20 mm, t = 1.5 mm, w = 29 mm), a power of 10 W and thermal conductivity λ = 690 W/m/K, a temperature difference of 7 K results. Cooling the crystal basis to 110 K should not be a technological problem even though the head transfer from the crystal to the cooled base will not be perfect.

The temperature distribution over the illuminated volume is shown in Figure 5.8. Actually shown is a lower quarter of the illuminated volume. The through thickness temperature gradient is found to be 0.06 K and the maximum temperature difference is about 1 K. From the slope of the thermal expansion coefficient it follows that the coefficient can be held below 1.7×10^{-8} K. From the through thickness temperature gradient a parasitic strain of 10^{-9} is estimated which is negligible (compared to the 10^{-5} bending strain). Likewise, the d-spacing difference for 1 K temperature difference of 2×10^{-8} is negligible compared to the bandwidth of 10^{-3}. Under actual beamline operation conditions it will probably not be possible to keep the crystal temperature in the illuminated volume within a 1 K band around 120 K. But thermal expansion should be negligible even for a temperature band of ±10 K, in which case the cooling power could be maintained independently of the heat load.

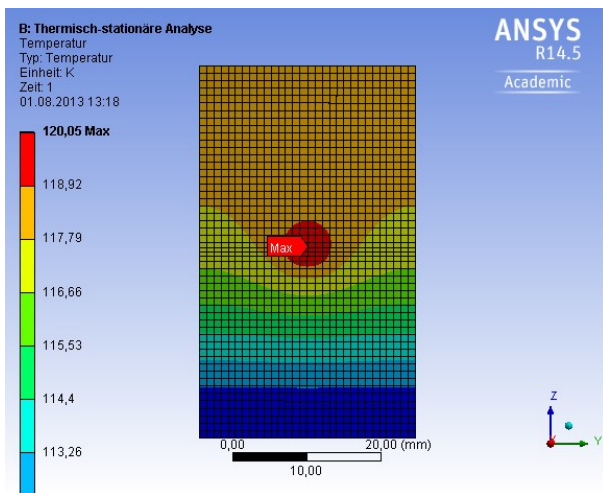**Figure 5.7: Temperature on monochromator front side.**
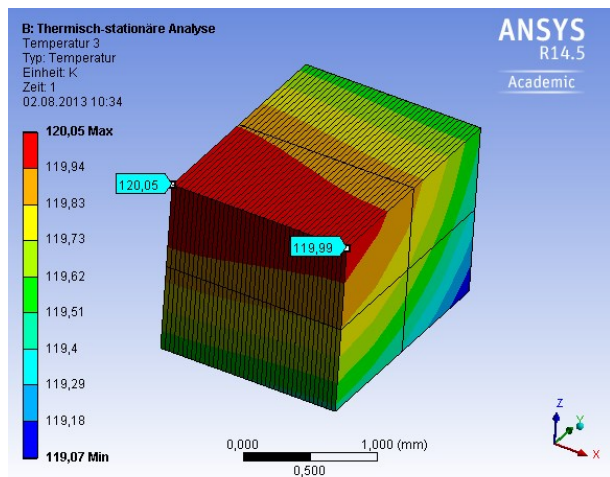**The incident beam size was 4×2.4 mm² (h×v).**

Figure 5.8: Temperature in the illuminated volume. A lower quarter of the illuminated volume is shown.

On the other hand, at room temperature heat load effects are expected to increase by about two orders of magnitude due to the combined effects of reduced thermal conductivity and increased thermal expansion. Then they are not anymore negligible within the uncertainty margin of the simulation. Cryogenic cooling is therefore the preferred option and will be pursued for the monochromator design.

While cryogenic cooling seems necessary, the relative small absorbed power seems not to justify liquid nitrogen cooling. Closed cycle refrigerator systems seem more appropriate as they are less likely to introduce vibrations. Considered systems are pulse tube cooling (PTC) to be employed at the European x-ray free-electron laser (XFEL) and "CryoTiger" implemented at the Swiss Light Source. In both cases cooling would be indirect and heat

from the crystal will be conducted by a Cu braid to a cold finger which is vibrationally isolated from the crystal mount. The large translation range of the second crystal would not allow for cooling. A relative Bragg angle difference of 2.55×10^{-4} would result between the cooled and uncooled crystals. At 40 keV the resulting angular offset would be $\Delta 2\theta = 30~\mu rad$. Over a distance of 50 m the offset is 1.5 mm which would require adjustment of the lateral position of some focusing elements.

Layout

A conceptual design of the double crystal monochromator is shown in Figure 5.9. The crystals will be mounted on positioning units consisting of a glancing angle selecting rotation stage, a cross tilt, and a translation to move the crystals out of the way of the wiggler beam if present. Since such a translation is required, two crystals might be mounted on each tower which could be optimized for different bandwidths. The first tower will be pre-aligned with the rotation axis in the beam while the second will be mounted to a long translation stage parallel to the beam. There are three popular ways to bent crystals: (i) pushing the tip of a triangular shaped crystal, (ii) four point bending, and (iii) moment bending. Here the last method is favored since this seems the only way to realize reliable boundary conditions by "double T" shaped crystals.
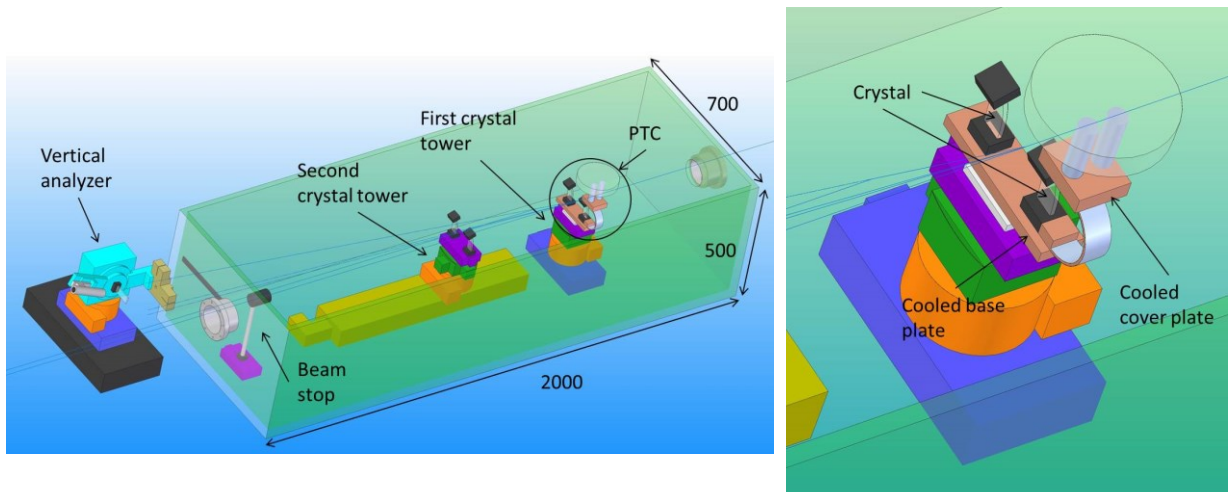

Figure 5.9: Conceptual design of the IVU-monochromator.
Left: Overview including the vertical analyzer. The beam travels from right to left.
Right: Cryogenic cooling of the first crystals by a PTC unit and Cu braid is sketched. Details of the bending mechanism are omitted.

A minimum beam offset of 20 mm is required by safety regulations for a Bremsstrahlungs stop. The actual offset will be around 24 mm and manually adjustable. For this horizontal offset the downstream displacement of the second crystal will be 245 mm at 40 keV, 919 mm at 150 keV, and 1224 mm at 200 keV. A water cooled beamstop is placed at the end of the tank. Since the center of the monochromatic wiggler beam will be at least 25 mm above the IVU beam, the beamstop would not need to be motorized. It is planned to mount a vertical crystal analyzer downstream behind the monochromator to optimize the bending of the first crystal.

5.1.2 Wiggler monochromator

Since implementation of the wiggler is planned only for stage III, a detailed description is beyond the scope of this report. However, due to the large horizontal beam size the only option is a Laue-Laue monochromator with vertical diffraction plane. The high energy limit will be around 150-200 keV while the low energy limit will be set by the crystal thickness and the achievable minimum distance between the crystals. The vertical beam offset will be around 30 mm to keep the vacuum tank reasonably short.

5.1.3 Other white beam components

Most upstream in OH1 is a unit for diagnostic of the frontend vacuum which also contains a diamond window separating the machine from the beamline vacuum. In phase I the monochromator from the side station, as described in section 6.1.1, will be operated in parasitic mode from the IVU beam. Downstream of the IVU-monochromator a unit is foreseen to position CRLs, a retractable fluorescence screen that also serves as beam position monitor, a Bremsstrahlungs stop which is a critical safety component, and a secondary beam shutter (NBS).

5.2 Monochromatic beam optics (OH2 & CRL enclosure)

For high-energy x-rays the attenuation in air is small and the scatter from extended air paths sufficiently upstream of the sample position is generally negligible (and could be further reduced by He flight paths or coarse vacuum). Also, ozone production by monochromatic high-energy beams has not been a significant problem at existing high-energy beamlines. On the other hand, the operation of x-ray instrumentation under UHV conditions poses severe complications. Furthermore, minimizing the number of optical components in the white beam optics hutch will also minimize the need to enter into the hutch and therefore improve beam stability by keeping the beam on the monochromators. A monochromatic optics hutch (OH2) is therefore proposed downstream of OH1. The positioning of all in-line components in OH2 needs to be compatible with the undulator and wiggler operation modes. Therefore the vertical off-set of the wiggler beam could be exploited or components would need to be translated.

A diamond window will be installed at the entrance into OH2 to separate from the OH1 UHV vacuum. The main in-line component in OH2 will be an optional high resolution monochromator which will cut down the bandwidth from the Laue-Laue monochromator by about a factor of ten (see Figure 5.10). The large distance of 40 m to the sample position in EH3 will enable focusing with low convergence and thus provide high reciprocal space resolution. The monochromator will consist of two (most likely Si 111) channel cuts in non-dispersive setting providing a narrow bandwidth beam without changing the beam position. The required accurate angular positioning of the channel cuts will be achieved by commercial Kohzu tangent-bar stages (KTG-15D). Fast switching from medium to high resolution diffraction will be possible by translating the channel cuts in and out of the beam. All positioning stages are commercially available.
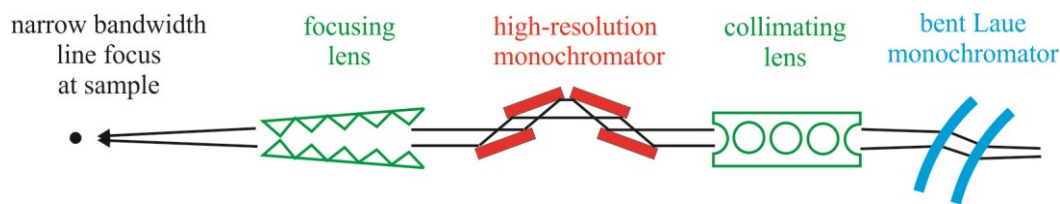
Figure 5.10: High-resolution reciprocal space optics
as implemented at the APS 1-ID beamline (Shastri et al., 2007).

Upstream of the high resolution monochromator will be collimating CRLs and downstream a mount for focusing CRLs. The source limited focus sizes in EH2 and EH3 will be 97 × 4.1 μm and 120 × 5.0 μm (h×v), respectively. The vertical and horizontal positions of the focusing CRLs should be used to tweak the position of the focused beam as measured by a position sensitive detector close to the focal point. Additional components foreseen for OH2 are beam defining slits, intensity monitors (ion chambers or Si pin diodes), beam attenuators, a fast shutter, and an energy monitor. Energy monitoring to a precision of $\Delta E/E < 10^{-4}$ has been achieved by monitoring the attenuation of a transmission K-edge foil by ionization chambers. The development of energy monitors at arbitrary energies is desirable. Finally, a secondary beam shutter will be placed at the downstream end of OH2 such that the downstream inline hutches are accessible when beam is delivered to the side station.

The beam will be transported to the experimental hutches in a lead shielded flight tube of 100 mm inner diameter under fine vacuum and with suitable windows (e.g. Kapton or aluminum). The 100 mm diameter is required to cover both the wiggler beam (upward off-set) and the undulator beam (inboard off-set).

The CRL enclosure will provide another location for focusing in-line optics. The source limited focus sizes in EH2 and EH3 will be 24 × 1.0 μm and 43 × 1.8 μm (h × v), respectively.

5.3   EH2: "roll-in" station

The "roll-in" station has a length of 8.2 m and width of 6 m. The station can be served both by the wiggler and IVU. It is intended for bulky instruments that require only limited positioning such as large beam tomography instruments or sample synthesis environments. The initial instrumentation will therefore be rather basic and consisting of beam conditioning by slits and an intensity monitor. A large area detector (probably a Perkin Elmer a-Si detector) and beam stop are foreseen.

Efficient operation requires a slow turn over where changes of instrumentation are restricted to periods when no user beam is delivered and installed instruments remain in place for several weeks or months and are used intermittently. Since the hutch is quite spacious simultaneous installation of two instruments might be possible along or transverse to the beam. Delivery of the IVU beam into EH3 must be possible by simple manipulations. Short air paths are tolerable but most of the EH2 length should be covered by coarse vacuum flight tubes if beam is taken into EH3.

If required, a replaceable table with CRLs could be installed towards the end of EH2 to optimize divergences and focus size for experiments in EH3.

The last component in EH2 will be a secondary beam shutter with 100 mm aperture centered on the undulator beam. The 100 mm diameter would allow combined use with the SAXS detector at the end of EH3.

5.4 EH3: Diffraction station

The diffraction station is considered the main station in view to the materials characterization mission of the beamline. It is the largest station and located at the downstream end of the beamline which has several advantages. First, the large distance from the source enables both a wide unfocussed beam and sub-micron focusing. This is required for "zoom-in" data acquisition. Second, the station will be accessible while experiments are performed in the downstream "roll-in" station. Since combination of techniques is another objective, it is by definition that the station needs to accommodate several sample positioning devices and detectors. It will therefore be crucial to have maximum access to the hutch for setup, development and maintenance.

The goal to combine experimental techniques and the necessity to make efficient use of beam conditioning elements and in particular detectors suggests to mount complementary sample positioning units on rails perpendicular to the beam such that each can be combined with all beam conditioning elements and detectors. To minimize the effort to setup experiments and reduce experimental uncertainties, critical components should remain "pre-aligned" when they are not in use. Attention will be paid to reproducible repositioning and reserved parking positions such that the components can remain fully wired (power and control). In particular the transportation of detectors between hutches has proven to be disruptive to efficient operation. The principal layout of the hutch is sketched in Figure 5.11.
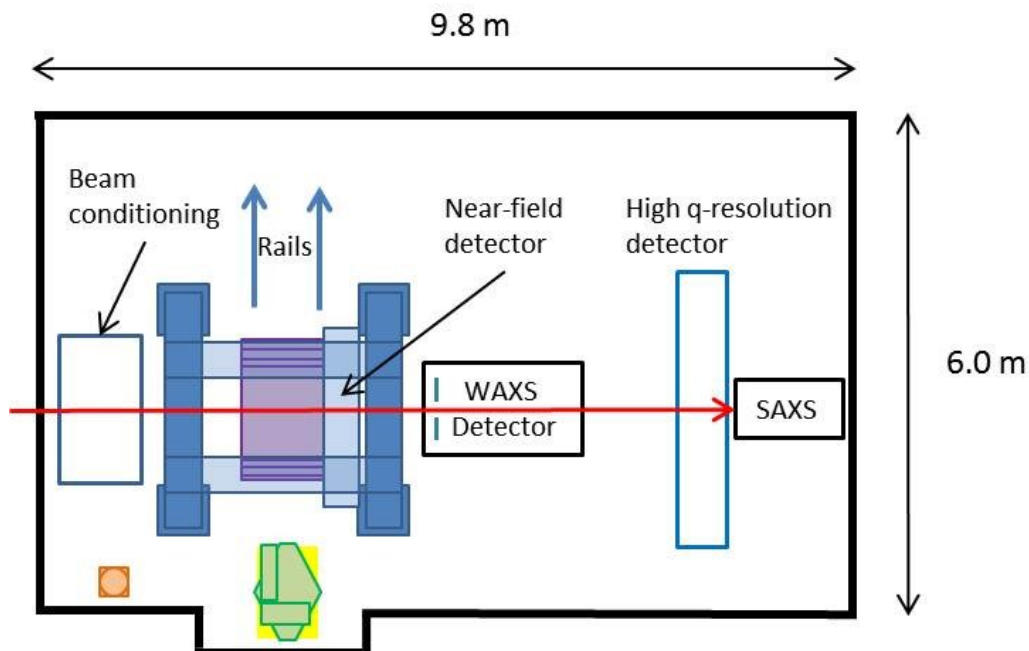

Figure 5.11: Layout of the diffraction station (EH3).
A frame construction around the sample position is indicated in blue that would hold near-field detectors and auxiliary equipment. The interface diffraction instrument (purple) is centered on the beam, while the parallel-kinematic table (yellow) is moved to the inboard end of the rails. The Eulerian cradle (green) is mounted on the table while the heavy load air-bearing table (brown) is moved to a parking position.

5.4.1 Conditioning optics

Most conditioning optics will be installed on an optical table at the hutch entrance. The support structure must provide long term stability and the thermal expansion should be matched to the sample positioning units. A granite plate on a steel support seems an adequate realization. The following components are considered:

(i)   Primary and secondary slits. The slits should have linear encoders and scattering from the blades should be minimized for SAXS experiments. A compact design is particularly advantageous for the secondary slits since they may need to be placed close to the sample (and in some cases mounted onto the base support of the sample positioning units).

(ii)   Focusing optics. Primarily foreseen are CRLs that might initially be manually assembled. The distance to the sample position will be about 2 m resulting in a source size limited focus of 4.5×0.19 μm^2 (h $\times$ v). Horizontal focusing by a curved multilayer could increase the effective aperture by a factor of five while still retaining the source limited focus size. However, this would result in a horizontal beam deflection of several mrad which would need to be accommodated by all downstream components. While this will be possible, it is inconvenient and it is therefore proposed to start with focusing by CRLs.

(iii)   Beam position and intensity monitor. Given the narrow vertical source size and large distance to the source point, at least vertical beam position feedback should be anticipated. Beam position monitoring to sub-micron precision has been demonstrated by position sensitive ion chambers. The position monitor must be close to the sample but should be upstream of the fast beam shutter.

(iv)   Fast shutter. The fast beam shutter must cover the full central cone of the undulator, be high energy tight, and also provide opening times down to milli-seconds. Since it must be positioned downstream of the position monitor, it also must be compact and operate with minimum vibrations. Galvanometer based shutters fulfill these stringent requirements.

(v)   Auxiliaries. Foreseen are an alignment laser and scatter shield.

The order and selection of beam conditioning elements will depend on the particular experimental requirements. The elements must therefore be replaceable. For background critical experiments all unnecessary conditioning elements should be removed and replaced by an evacuated flight tube.

5.4.2 Sample positioning units

Complementary sample positioning requirements exist for bulk and interface diffraction. Bulk diffraction maybe subdivided into the required rotational degrees of freedom: none for powder diffraction (but at least one for diffraction contrast tomography and pole figure coverage), one and more for single crystals in combination with area detectors that cover complete diffraction rings or only narrow reciprocal space regions, respectively.

It is therefore suggested to place a sample positioning unit for interface diffraction and a parallel-kinematic support on rails perpendicular to the beam.

Interface diffractometer

The interface diffractometer will be a copy of a device which has been used successfully at the P07 physics hutch for grazing incidence diffraction and reflectivity measurements. The hallmark design feature is a large swing frame that pivots around an axis which is aligned on beam height. The incidence angle on interfaces can be selected to 200 nrad precision. Stacked on the frame are a translation parallel to the precision tilt axis and three rotations and translations such that a sample can be oriented and aligned to the rotation axis. The instrument and key performance parameters are shown in Figure 5.12.

Since an operational interface diffractometer is available at EH2 (P07), it is considered second priority for P21. On the other hand, since no design work is required it should be installed as soon as appropriate beamline infrastructure is available.

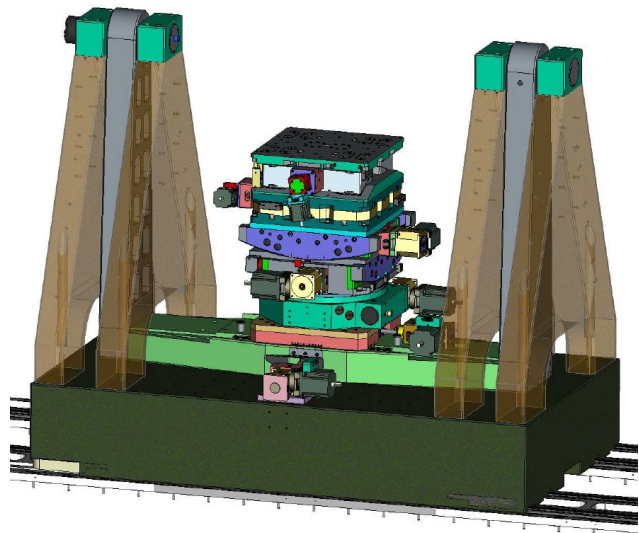| Reproducibility of θ tilt angle	200 nrad
z-stage:	+/- 10 mm, 200 kg load
xy-stage:	+/- 25 mm
x- & y-axis and θ swing tilts:	+/- 5°
φ rotation:	+/- 180°
Sample stack:	+/- 30 mm

Figure 5.12: The interface diffractometer and key performance parameters.
The order of components in the table reflects their vertical arrangement (courtesy by Huber).

Bulk diffraction diffractometers

The support for the bulk diffraction positioning units should provide the stability to operate an air-bearing precision rotation stage to the limits of its tight specifications (2.4 μrad tilt error, 20 nm axial error). Furthermore, it should provide vertical motion and tilting around axes in the horizontal plane (to align the horizontal ω-axis of an Eulerian cradle and the vertical rotation axis of the air-bearing rotation stage perpendicular to the beam). The positioning requirements can be realized by a three leg support which however is unlikely to provide the required stability under the expected load variations. Therefore a support based on parallel-kinematic construction is preferred. Sample environment that does not need external rotation axes (such as the air-bearing load frame presented in section 5.4.3) could be mounted directly to the support unit. In addition two diffractometers will be available to be mounted on

the support unit as detailed below. Reserved positions will be provided where the goniometer units can be parked without disconnecting cabling.

A vertical high precision rotation axis will be provided by an air-bearing stage. The foreseen axial load capacity is 100 kg and slip rings for electrical lines and possibly liquid and gas supply are considered. The specifications are rather complementary to the air-bearing stage that is part of the P07 grain-mapper which only supports 20 kg axial load and does not provide slip rings or rotary unions. The vertical rotation axis will be used for powder- and single-grain diffraction, and for the secondary imaging techniques (attenuation and diffraction tomography). Ultimate angular precision is not required, about 0.01° should be sufficient. On top of the rotation stage an XYZ positioning unit will be mounted. The high precision rotation axis is considered first priority. However, since the timely delivery of the interface diffractometer should not be problematic, performance should not be compromised to reduce design time.

Alternatively, a large Eulerian cradle could be mounted to the support unit. The horizontal ω-axis will enable exploitation of the narrow vertical source size. An XYZ-positioning unit will be mounted on top of an air-bearing φ-circle and still leave a working distance of about 130 mm to the beam. The air-bearing φ-stage will enable sample rotation with micrometer run-out at fixed ω and χ settings. While the sphere of confusion will be significantly larger, a precise φ axis will be very beneficial for imaging methodologies. Furthermore, the sphere of confusion could be reduced by calibration and a look-up correction table. The Eulerian cradle will be used for high-resolution reciprocal space mapping where selected reflections will be centered on medium size detectors, for diffraction imaging modes that require a tilted rotation axis, and multi-purpose reciprocal space exploration experiments. Alternative designs will be considered that could reduce the sphere-of-confusion. Due to the complexity, the three circle diffractometer is considered third priority. Conceptual designs of the air-bearing stage and Eulerian cradle mounted to the parallel-kinematic support are shown in Figure 5.13 and Figure 5.14, respectively.
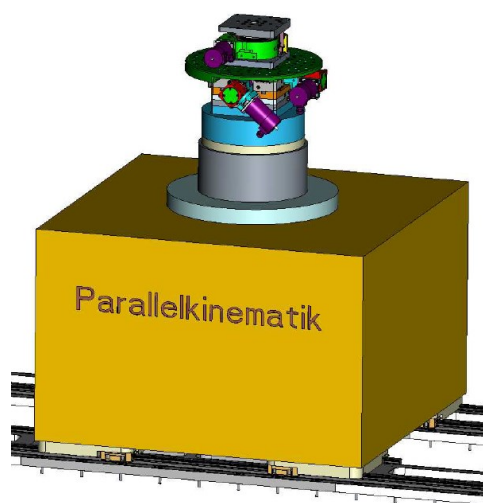

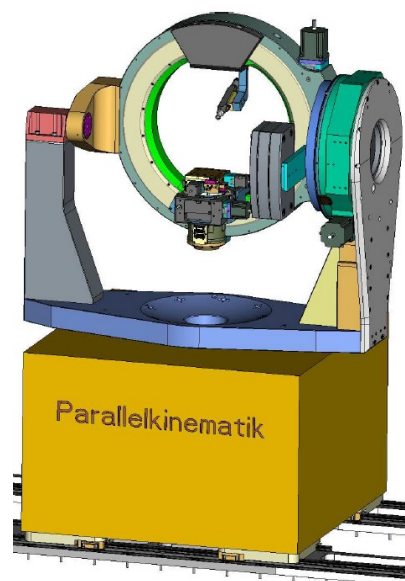**Figure 5.13: Design status of the precision vertical rotation axis (courtesy by Huber).**

Figure 5.14: Design status of the Eulerian cradle (courtesy by Huber).

5.4.3 Sample environments

In situ and *in operando* diffraction experiments are a common goal for all user groups and respective sample environments will be of critical importance. Even disregarding constraints arising from the diffraction methodologies, a wide variety of manipulators are required to reproducibly apply external stimuli such as chemical environment, mechanical load, temperature, high voltage, etc. and combinations thereof. Accommodation of constraints imposed by diffraction methodologies further complicate the situation. Furthermore, supplementary characterization methods such as digital image correlation to map surface strains may be added. Sample environments are often developed in close collaboration between beamline staff and expert users. This process is just starting for the P21 beamline and it must be expected that novel sample environments will be developed continuously. The proposed sample positioning units should facilitate such developments by tolerating relative high loads and large work distances, and by separating complementary diffraction methodologies. It is also anticipated that the existing overlap with instrumentation at the P07 beamline will facilitate the accommodation and operation of sample environments. Some relevant developments are described below.

In situ surface studies

1. In the last few years significant advances have been made for performing surface x-ray diffraction under relatively harsh conditions. In the field of model catalysts studied under semi-realistic operating conditions, it is planned to use a so-called *in situ* flow reactor chamber (UFO) (see Figure 5.15 a). Two such reactors are already available (one at PETRA III and one in Lund) with different gas flow capabilities, and some users have extensive experience with this set up, both at ID3 at the ESRF as well as on P07 at PETRA III. It is important in many cases that the gas lines between gas bottles and reactor are short.
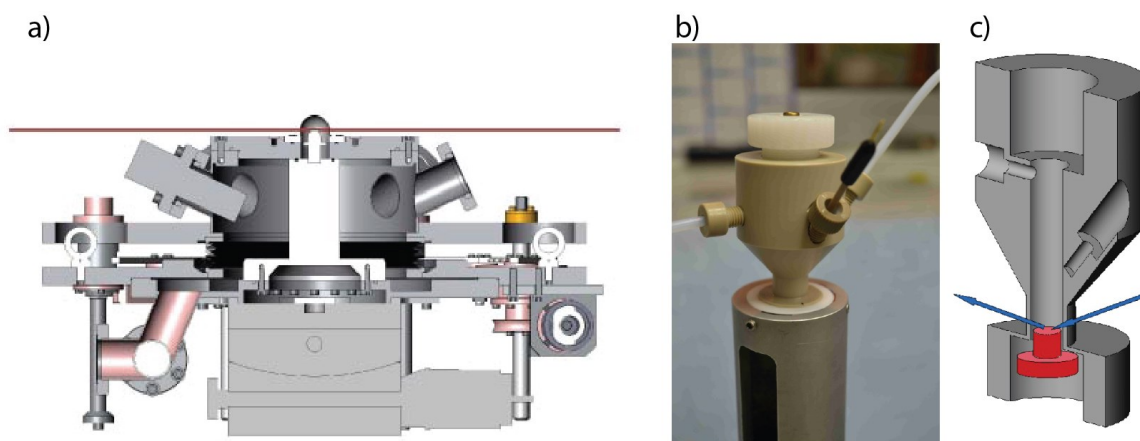
a)

b)

c)

Figure 5.15: Electrochemical Environment
a) UFO: Flow reactor for surface studies of model catalysts at work.
b) and c) electrochemical cell for surface studies of electrodes.

2. Further, an electrochemical environment is also planned which is at present directed towards corrosion studies, but could also be used for other electrochemical investigations. A cell currently present at ID3 at the ESRF is shown in Figure 5.15 b) and c). Some users have

experience with this set up from ID3 at the ESRF. In this case, the goal is to develop a valve switching system enabling switching between electrochemical liquids, directly from the online control system. Further, SAXS could be of importance, since periodic oxide pore structures can be grown electrochemically using the right conditions.

In situ bulk diffraction

1. Experiments aimed at bulk diffraction from technical catalysts under reaction conditions are also planned, possibly combined with IR spectroscopy. A cell has been developed in Lund for this purpose and is shown in Figure 5.16 a). The powder reactor has been tested at MAX-lab.

Figure 5.16: Bulk diffraction from technical catalysts
a) Flow reactor for powder diffraction from technical catalysts under operational conditions
b) Growth chamber for aerosol nano particles/wires to be studied using SAXS.

2. A novel method to synthesize nano particles/wires, aerotaxi, is currently being explored in Lund. An experimental setup to study this growth method using x-rays is shown in Figure 5.16 b). Here nanoparticles are produced in a heated area of the tube, and transported through the tube by an inert gas. The aim is to *in situ* study the particle distribution, size and shape along the growth tube using an x-ray beam, mostly using SAXS. At a later stage, metallorganic molecules relevant for nanowire growth on the particles may be added to the gas stream. The experimental setup is currently under development in Lund.

3. In view to the investigation of mechanical properties of bulk materials, two recent developments are mentioned. A stationary uniaxial load frame where the sample can be rotated under load is being developed by the Air Force Research Laboratory and PULSERAY. The stationary frame enables the recording of radiographs for an unlimited projection range up to 360°, a minimum near-field detector distance down to 8 mm, and the use of conical slit cells with a working distance down to 20 mm. A furnace and piezo-electric unit that also would enable high-cycle fatigue testing are under construction. A compact load frame has been designed that is compatible with a 50 mm working distance conical slit cell and has been operated on an Eulerian cradle with arbitrary orientation of the loading axis, see

Figure **5.17**. The frame is now operating in tension and compression enabling the investigation of low cycle fatigue.
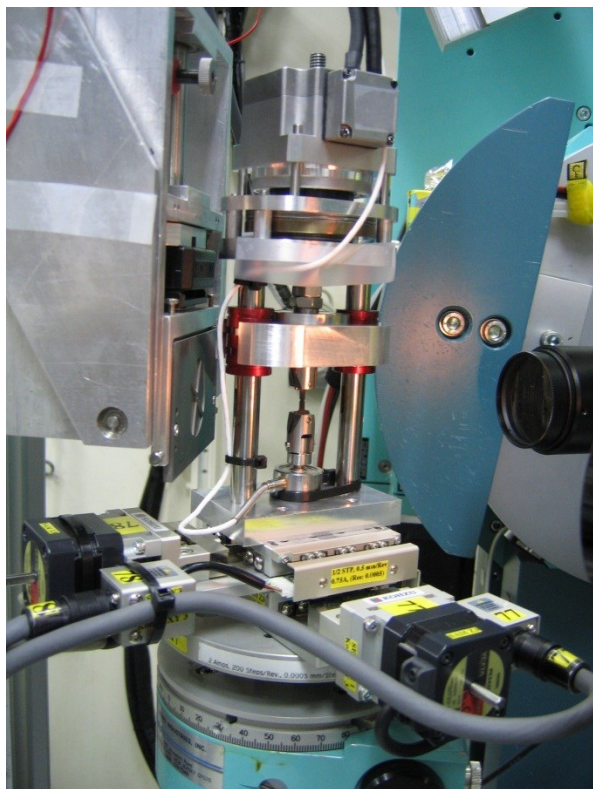
Figure 5.17: A compact load frame
that is compatible with a 50 mm working distance
conical slit cell and can be mounted to an Eulerian
cradle.

Other examples include instrumentation for the *in situ* characterization of cutting tools and thermo-mechanical test equipment for bulk metallic glasses. An ongoing collaboration aims at the development of furnaces that can provide fast thermal gradients.

These few examples already indicate the wide potential for future developments of sample environments. An active collaboration with the user community will be essential for the scientific productivity of the beamline.

5.4.4 Detectors

Near-field detectors

The term "near-field" is used for detectors that are positioned sufficiently close to the sample such that the position of a diffracting domain dominates the radial position on the detector, whereas angular shifts due to lattice strain are negligible (thus the usage of "near-field" is different from wave optics). These detectors will be mounted to an overhead frame around the sample positioning units which should significantly reduce the mounting and alignment time. Positional stability in respect to the beam can be monitored by using a semitransparent beamstop such that an outline of the direct beam is recorded on each image. The near-field detector should also be semitransparent such that diffracted beams can be recorded simultaneously on a far-field detector. Since suitable high-energy imaging detectors are not available commercially, it is suggested to build an imaging detector based on commercially available long working distance microscopy objectives (Mitutoyo) and investigate the suitability of existing custom designed imaging detectors. It is noted that the same detector that is used for diffraction imaging can also (at least initially) be used for in-line radiography.

Triangulation apertures are used to identify the position of diffraction events in the direction along the beam. They are described here since they also need to be placed close to the sample and form a "compound detector" together with a downstream far-field detector. A

conical slit cell is sketched in Figure 5.18 and preferred for single grain diffraction since it covers large fractions of several diffraction rings (Nielsen *et al.*, 2000). Spiral slit cells (see Figure 5.19) on the other hand only capture a relative small fraction of individual diffraction rings but work for all crystal symmetries and are therefore preferred in powder diffraction (Martins & Honkimäki, 2003).
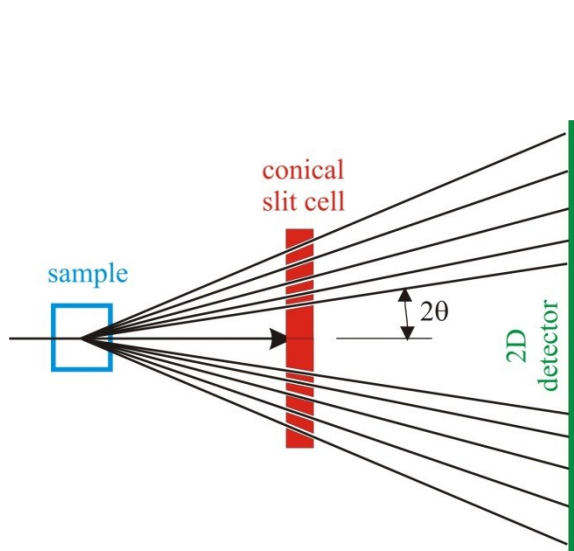

Figure 5.18: Principal of the conical slit geometry. Several almost complete diffraction rings are selected for a given crystal symmetry.

Figure 5.19: Spiral slit geometry.
Only small fractions of individual diffraction rings are transmitted but independently of the crystal symmetry (Martins & Honkimäki, 2003).

Medium resolution far-field detectors

Medium resolution far-field detectors are large area detectors that cover several complete diffraction rings and are at high energies typically positioned 0.5 to 2 m downstream of the sample. It is proposed to position a granite table downstream of the sample stages with two towers that can be translated along and perpendicular to the incident beam. Each tower will provide vertical positioning and rotation around a vertical rotation. The table will be placed on rails parallel to the beam such that an excessive length is avoided and that the table can be moved downstream to improve access to the sample. Moving the table upstream brings the first tower close to the sample.

It is proposed to operate two large area detectors, one that provides high frame rate and enables transmission of the direct beam to the SAXS detector and one that provides high dynamic range. For the first scenario a combination of two Perkin Elmer CMOS detectors 2923 is proposed as shown in Figure 5.20. Key performance parameters are that the active area is as close as 3 mm to one edge of the detector, the large number of pixels (23 Mpixels unbinned), high frame rate (70 fps in 2x2 binning), and significantly reduced image lag compared to a-Si detectors. For the second case a frame-transfer CCD matrix is considered under the condition that efficient scintillators will be available.
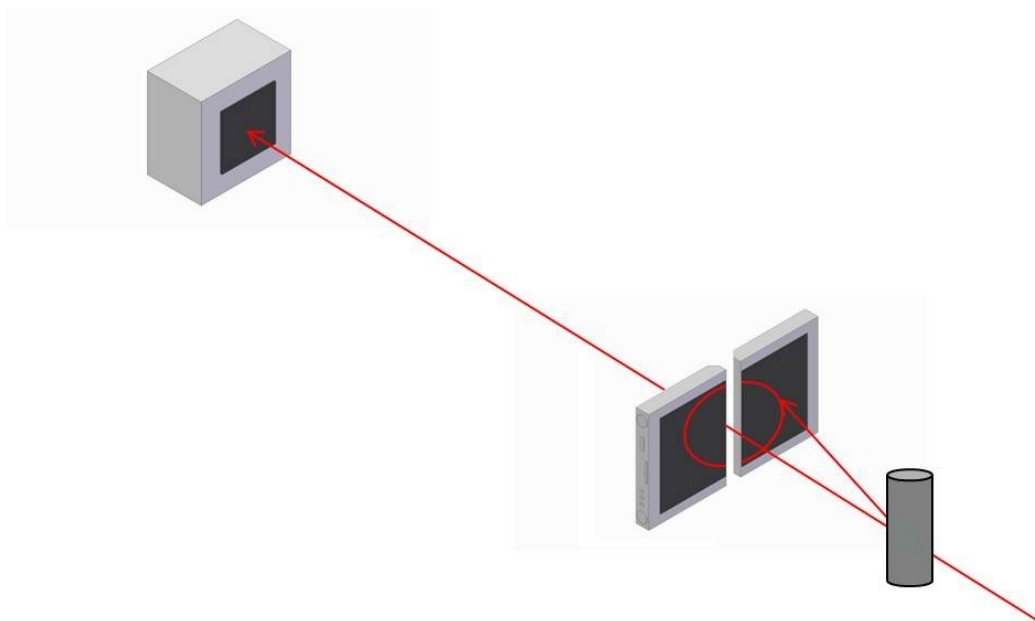
Figure 5.20: Simultaneous detectors for far-field and SAXS.
Two PE CMOS detectors are combined such that the direct beam is transmitted to a SAXS detector.

High reciprocal space resolution & SAXS

The high reciprocal space resolution detector will be mounted on a positioning frame downstream of the far-field detector table and about 4-5 m from the sample position. The positioning frame will cover about 2 m of travel in a plane perpendicular to the direct beam. The SAXS camera will be positioned at the very downstream end of the hutch.

The detector image area can be significantly smaller than for the far-field detectors and both applications benefit from smaller pixel sizes, ideally down to 20-30 μm which can be achieved with structured scintillators. Pixel-detectors will have larger pixel size but promise high frame rates, and unprecedented dynamic range.

Point detectors and auxiliary probes

A scintillation counter and Si PIN diode are foreseen to record reflectivity scans with the required dynamic range of many orders of magnitude. Si PIN diodes will also be incorporated into beam stops and used for alignment and intensity monitoring.

An energy dispersive CdTe detector should be available for monitoring fluorescence from samples and knife-edge patterns to characterize focus profiles.

It is expected that auxiliary probes will be operated simultaneously with x-ray measurements. So far, candidates are digital image correlation and/or a laser extensometer, and infra-red spectroscopy.

5.4.5 Data acquisition, reduction, visualization & evaluation

Data acquisition and reduction software will be crucial for the scientific productivity of the beamline. Particular challenges are the synchronization of simultaneously operated

detectors, sample rotations, combined translational positioning, and external events. Due to the anticipated sub-second exposure times "on the fly" image acquisition is mandatory since start and stop sequences not only add extensive overhead time but also impact the accurate sample positioning. Due to uncontrollable network latencies, the synchronization cannot be software based but most be controlled by a hardware clock. Data logging must be automated and accessible on-line. Data reduction and visualization must be available on-line such that the progression of an experiment can be adapted. This also necessitates at least preliminary data evaluation. Scientific beamline staff must be closely involved in the software development but additional support by a professional software developer is required. The software development has to be coordinated with the experiments control group.

6   P21.B Side-station: broad band diffraction

6.1   White beam optics (OH1)

Two different monochromator concepts are considered for the side station. The first, a double bounce monochromator which can be operated at three different energies and which allows a medium bandwidth. The second, a double crystal multilayer monochromator operating at fixed energy and large bandwidth.

6.1.1   Double bounce monochromator

The bouble bounce monochromator has a fixed offset of 1.28 m, which results in a separation of about 17 m of the two crystals. Scattering angles are chosen to obtain 100 keV with a Si(311) reflection, which is 4.34 degrees. By exchanging the (311) reflection against (111) or (220) reflections, energies of 52 and 82 keV are obtained. However, since the (222) reflection of Silicon is not completely forbidden and the (440) reflection is allowed, these two energies cannot be used for experiments where a high suppression of higher harmonics is needed. For the (311) reflection a suppression of more than six orders of magnitude is expected. A further but smaller tuning of the energy can be accomplished by translation of the second crystal in beam direction. Employing this scheme an energy tune of +/- 6 keV can be obtained for the (311) reflection. This allows reaching the next harmonic of the undulator in case of unfavorable conditions.

The bandwidth of the monochromator will be increased by either bending the monochromator crystal or by applying a thermal gradient. Since the increase of bandwidth also increases the horizontal beam diameter, the maximum tolerable bandwidth is 0.1 %. For the thermal gradient crystal optics a bandwidth of 0.1 % can be obtained for a 5 mm thick crystal with a rocking width of 8 arcsec. which will have a reflectivity of about 90 % (see Figure 3.6). Alternative schemes to increase the bandwidth will be considered.

In phase I the side station and the diffraction station will use the same undulator beam, consequently the sidestation monochromator needs to be sufficiently transparent. The transmission of a 2 mm bend Si crystal is always above 85 % for energies higher than 50 keV. When crystals with larger thicknesses are employed alternating operation of the side station and the main station need to be considered during phase I. The heatload deposited from the U29 undulator beam (1 mm², at a distance of 80 m) on a 2 mm Si crystal behind a 100 µm Cu-filter is about 1 W. Water cooling shall be sufficient to keep the temperature within a few degrees C stable.

6.1.2   Double crystal multilayer monochromator

The double crystal multilayer monochromator comprises two dispersive Si(111) crystals separated by a short distance of approximately one meter with a multilayer in between these two crystals. The multilayer serves to invert the photon momentum distribution such that the second crystal reflects all wavelength coming from the first crystal, similar to a non-dispersive setting. This would not be the case in the dispersive setting without the multilayer. This setup has the advantage that the beam broadening is limited to the distance between the two crystals. Since this distance is only about 1 m a higher bandwidth can be obtained with the

double layer multilayer monochromator without spoiling the horizontal beam cross section. However, the demand on the multilayer quality is significant. For the small scattering angles at high energies a multilayer needs to have an evenness better than a few μrad over distances of 50 cm and a large bandwidth. Multilayer reflectivities at x-ray energies of 100 keV and the monochromator concept shall be tested in the future.

The back draw of this setup is the fixed energy close to 100 keV. Thus it might be preferable to combine this setup with the double bounce monochromator. One should note, however, that the direction of the incoming beam onto the sample is different for the two cases. Consequently, switching from one monochromator to the other requires a significant change of the beamline setting.

The bandwidth is tunable depending on the rocking width of the two Si crystals which can be chosen by the thermal gradient or the bending radius. With a 0.2 mrad rocking width of the two crystals a bandwidth of 1 % can be achieved. The accompanying horizontal beam spread will be 0.3 mm in this case.

6.2   Monochromatic beam optics

For certain applications focusing of the beam might be necessary, in particular in the vertical direction, which is unaffected by the monochromator optics. Here 1d lenses will be foreseen to be installed in either the OH1 or OH2 hutch. Using e.g. about 100 Al lenses with 0.1 mm radius 10 m in front of the sample a vertical beam size of 1.6 μm can be achieved at 100 keV. The broad band width however limits the focal size. When the double bounce monochromator is used, horizontal focusing is limited by the divergent beam from the mono which does not conserve the source size.

6.3   EH1: Side-station

6.3.1   Diffractometer

The diffractometer in the experimental hutch consists of three parts, the incoming beam table, to prepare and diagnose the beam impinging on the sample, the sample table that carries and moves the sample and the detector table, which positions the various detectors in the diffracted beam. The incoming beam table carries beam attenuators, slits to adjust the beam size, pinholes close to the sample to remove air scattering and clean up the beam, a monitor to determine the incoming intensity, and a monitor to detect the position of the incoming beam. Optional, focusing lenses can be mounted on this table if required. However, the standard location for lenses shall be the optics hutch OH2. All components will be mounted on an X95 optical bench, for easy adjustment of the position along the beam. The table shall be movable in height and in transverse direction to the beam and be based solid on the ground for high stability.

The sample table needs to be able to fulfill a multitude of duties, carry heavy loads, cover large range of angle space, move fast and be non-magnetic for high magnetic field work. This is not achievable with one single setup. Consequently, the sample table shall provide a common basis for all requirements, which is providing the basic sample orientation angles, 360 degrees for omega, +/- 10 in χ and φ, sample translation in 3 dimensions +/- 10 mm and

positioning of the sample in the beam. The sample table needs to be able to carry weights of up to 600 kg, and be manufactured of non-magnetic material, like the incoming beam table and the detector table. On top of the sample table a number of add-on instruments shall accomplish the tasks that cannot be done by the common basis. E.g. an Euler cradle shall be mountable for crystallographic work, a table with an automated sample changer will be provided. This will allow a high sample throughput in particular for PDF applications. The sample mount will be standardized as much as possible and common solutions with other beamlines at PETRA III will be investigated.

Connected to the sample stage is a 1.5 m detector arm that can be rotated horizontally and vertically which carries the analyzer stage together with the point detector. When working with the area detectors the arm will be moved out of the beam in the vertical. This arm might be extended to carry multiple detectors for low noise measurements.

The detector table carries the large area detector and the pixel detector. Horizontal and vertical motions are needed to cover the respective ranges of momentum space, which is about 10 $\mathring{A}^{-1}$ in the vertical and 40 $\mathring{A}^{-1}$ in the horizontal at 100 keV. In order to adjust the resolution and to be able to switch between the detectors by remote control the detector table will be made movable along the beam direction with a long translation.

6.3.2 Sample environments

The use of various sample environments for *in situ* observation of functional materials is the heart of the beamline. Thus the park of the beamlines sample environments will never be complete, but grow with the complexity of the experiments. While very specialized devices are usually developed and brought by the user groups, e.g. levitation furnace, high temperature stress rig or sputter chambers, the standard devices will be provided with the beamline. As a starter package a number of devices will be available from the DORIS beamline BW5.

These include:

- Large vacuum furnace T<1600 degree C,

- Vacuum light-bulb furnace T<1000 degree C,

- Mirror furnace T<700 degree C,

- Displex cryostat 6.5<T<450 K,

- Displex cryostat 10<T<280 K,

- Magnet cryostat H<10 T, 1.5<T<300 K,

Furthermore it is foreseeable that further high temperature furnaces working under various atmospheres will be needed. Exact specification shall follow user demands.

6.3.3 Detectors

The work horse for pair distribution function (PDF) measurements and any kind of diffraction on polycrystalline material will be the large area detector. For first experiments a Perkin-

Elmer amorphous Si detector is already available. A large area detector with less afterglow and a larger dynamic range would be beneficial.

Pixel detectors are so far available only as prototypes with limited areas of a few square centimeters. This is highly useful for e.g. diffuse scattering maps in between a set of Bragg reflections. Once these detectors reach a certain degree of maturity they will be extremely useful for collecting diffuse scattering phenomena. In larger sizes they could be used to complement the large area detector and allow low noise measurements of PDF and nano-diffraction. One should carefully observe the further development of these devices.

For low noise measurements when a sensitivity of more than eight orders of magnitude is required, a point detector together with an analyzer crystal is the only choice until now. With such a setup all fluorescence and Compton scattering can be efficiently suppressed. Furthermore, the energy resolution allows to determine if the signal is contaminated by higher harmonic scattering. Thus point detectors together with analyzer crystals will be among the core equipment of the side-station. Scintillation counters are very reliable and simple to use and can be obtained in any required size. For measurements in magnetic field solid state detectors are required and an electrically cooled Ge detector will be the first choice.

6.3.4 Data acquisition & reduction

At the side-station the DESY Photon Science software Spok and Online will be used for instrument control and data acquisition of point detector data. Data taken with area detectors require additional software, e.g. QXRD for the Perkin-Elmer large area detector. Programs to convert 2d-detector data in Q-space are under development and shall be implemented in Spok and Online as much as possible. More specialized data analysis programs willl be provided by user demand.

7 Timeline

2013		2014				2015				2016	
III	IV	I	II	III	IV	I	II	III	IV	I	II
		PETRA shutdown					Front end install.		Machine modifi-cation		
		Hall East: Construction			Infrastructure						
							OH1: construction				
							EHs : construction				
									Beamline infrastructure		
									Optics: Installation & commissioning	commis-sioning	
Monochr. for IVU: design		Call for tender	Fabrication						Installation & commission.	commission.	
Monochr. for EH1: design		Call for tender	Fabrication						Installation & commission.	commission.	
Instrumentation for EH3: design		Call for tender	Fabrication	1st priority: vertical precision rotation axis					Installation & commission.	commission. & user mode	
Instrumentation for EH1: design		Call for tender	Fabrication	2nd priority: interface diffractometer					Installation & commission.	commission. & user mode	
				3rd priority: three circle diffractometer							
		Detectors: Purchase & integration in data acquisition software								commission. & user mode	

Figure 7.1: Detailed time chart
of the construction of the experimental hall and the phase I beamline development. First availability of beam is indicated by the vertical red line.

Status/completed	Task	Group
ongoing	*Design machine vacuum chamber*	*MVS*
ongoing	Call for tender IVU	FS-US
ongoing	Construction of phase I front end	FS-BT
ongoing	Specification of beamline & lab infrastructure	P21/FS-TI
ongoing	Design of IVU monochromator crystals	P21/ZM1
10/2013	Specification of beamline hutches	P21/FS-TI
1/2014	Design of in-line & side-branch monochromators	P21/ZM1 or external company
1/2014	Design of EH1 & EH3 instruments	P21/external company
5/2014	Call for tender in-line & side-branch monochromators	P21
5/2014	Call for tender EH1 & EH3 instruments	P21
7/2014	Order detectors	P21
4/2015	Design and order EH1 & EH3 beam conditioning and detector support	P21
6/2015	Installation of front-end components	FS-BT
8/2015	Construction of beamlines hutches	external company
11/2015	Commissioning of beamline infrastructure	P21
1/2016	Installation of OH1 components	FS-BT
2/2016	Install & test monochromators	P21
2/2016	Install & test EH1 & EH3 instrumentation	P21
2/2016	Start commission beamline	P21

Table 7.1: Selected phase I beamline construction tasks.

8   List of figures

9 List of tables

10 List of abbreviations

11 References

Balewski, K., Brefeld, W., Decking, W., Franz, H., Röhlsberger, R., Weckert, E. (edts) (2004) PETRA III TDR.

Keitel, S., Retsch, C.C., Niemöller T., Schneider, J.R., Abrosimov, N.V., Rossolenko, S.N., Riemann, H. (1998) *Nuclear Instr. Meth.* A **414**, 427-430.

Lengeler, B., Schroer, C.,Tümmler, J.,Benner, B., Richwin, M., Snigirev, A., Snigireva, I., Drakopoulos, M., (1999) *J. Synchrotron Rad.* **6**, 1153-1167.

Lienert, U., Schulze, C., Honkimäki, V., Tschentscher, T., Garbe, S., Hignette, O., Horsewell, A., Lingham, M., Poulsen, H.F., Thomsen, N.B., Ziegler, E. (1998) *J. Synchrotron Rad*. **5**, 226-231.

Lienert, U., Poulsen, H.F., Honkimäki, V., Schulze, C., Hignette, O. (1999) *J. Synchrotron Rad*. **6**, 979-984.

Martins, R.V., Honkimäki V. (2003) *Textures and Microstructures* **35**, 145-152.

Nielsen, S.F., Wolf, A., Poulsen, H.F., Ohler, M., Lienert, U., Owen R.A. (2000) *J. Synchrotron Rad.* **7**, 103-109.

Rütt, U., Schulte-Schrepping, H., Heuer, J., v. Zimmermann, M., (2010) *Proceedings oft he 10th International Conference on Synchrotron Radiation Instrumentation*, 748-751.

Shastri, S.D., Almer, J., Ribbing, C., Cederström, B. (2007) *J. Synchrotron Rad*. **14**, 204-211.

Tanaka, T., Kitamura, H. (2001) *J. Synchrotron Rad*. **8**, 1221-1228.

Zhong, Z., Kao, C.C., Siddons, D.P., Hastings, J.B. (2001) J. Appl. Cryst. **34**, 504-509.

12 Appendix

A1) Description of the beamline gas supply system

The gas supply system should enable the delivery of gases of various chemical properties into the three proposed experimental stations. The plan presented in Figure 12.1 has been developed according to standards of the responsible technical infrastructure group (FS-TI). In particular, gas bottles must be installed in fire resistant and ventilated safety cabinets. Gases are classified into five groups (i) inert, (ii) flammable, (iii) oxidizing, (iv) toxic, and (v) very toxic. Exclusions exist for the common storage of gases from different groups in the same cabinet. Furthermore, specific regulations apply for valves and sensors. Therefore it is expected that up to three separate cabinets may be required for specific experiments. Since gas cabinets need to be ventilated and maintained, a mobile cabinet has been developed by FS-TI to accommodate peak demand. The mobile gas cabinets can also be operated within experimental hutches if appropriate ventilation is provided. Operating mobile gas cabinets inside of experimental hutches minimizes the length of the supply lines but complicates the setup of experiments.

The proposed system consists of two permanent cabinets (XXL and XL sizes for four and three gas bottles, respectively) which are located at the back side of OH2, and a connecting station for a mobile gas cabinet between OH1 and OH2. A schematic of the supply lines from these distribution points to the three experimental hutches is shown in Figure 12.1. Furthermore, all experimental hutches will be equipped with an additional chicane for ventilation of two mobile gas cabinets. Supply of gases to laboratory rooms is not addressed by the present plan.
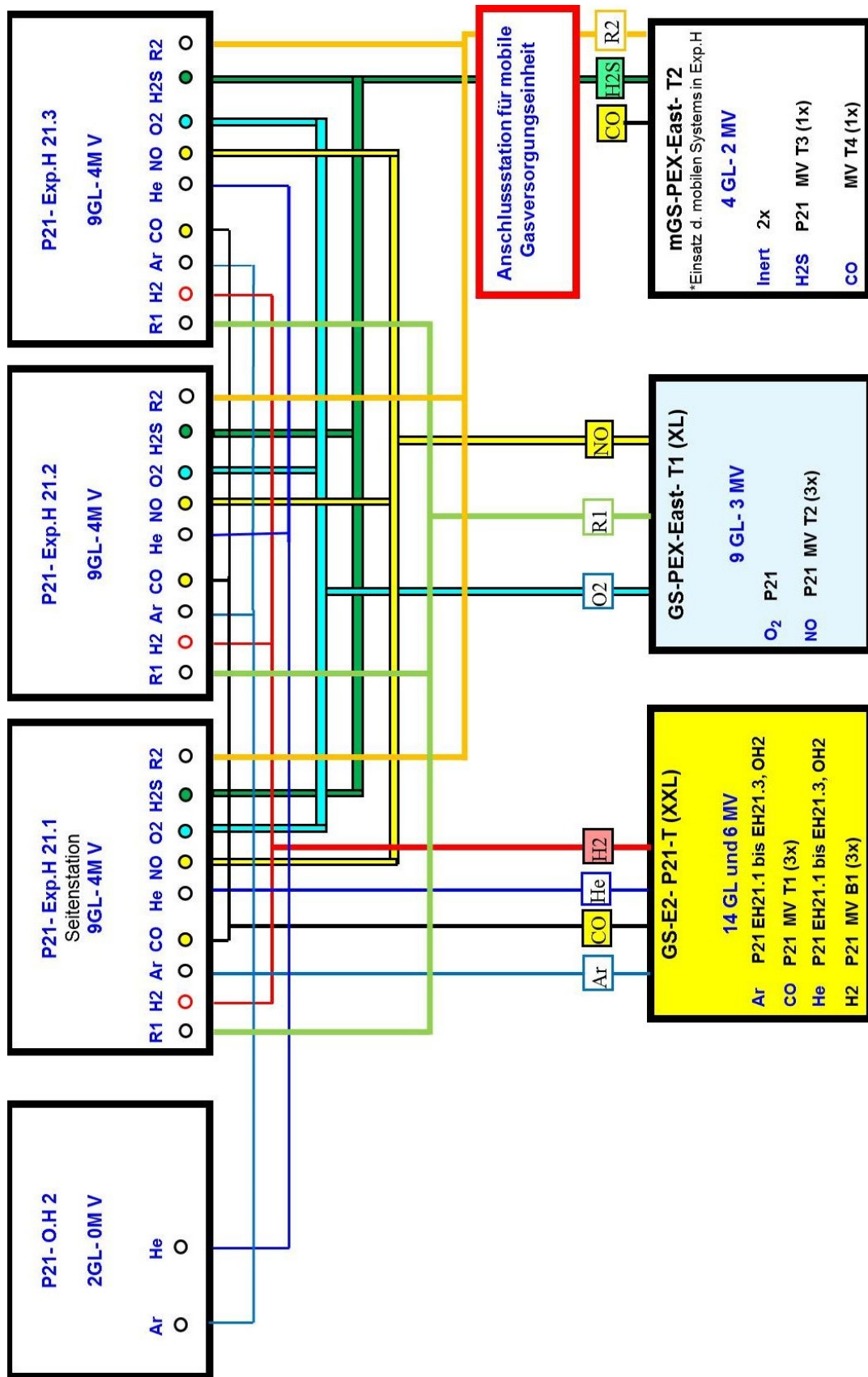
Figure 12.1: Gas supply system for P21 experimental stations.